Out-of-plane measurements of the fifth response function of the exclusive electronuclear response

S. M. Dolfini,[1,2,*] R. O. Alarcon,[2] H. Arenhövel,[3] R. Beck,[1,†] A. M. Bernstein,[4] W. Bertozzi,[4] W. Boeglin,[4,†] S. Boffi,[5]
J. R. Comfort,[2] D. Dale,[4,‡] G. Dodson,[4] K. Dow,[4] M. B. Epstein,[6] M. Farkhondeh,[4] S. Gilad,[4] J. Görgen,[2,§] M. Holtrop,[4]
D. Jordan,[4,∥] W. Kim,[1,¶] S. Kowalski,[4] R. Laszewski,[1] J. Mandeville,[1,**] D. J. Margaziotis,[6] D. Martinez,[2] T. McIlvain,[4]
R. Miskimen,[7] C. Papanicolas,[1,8] M. Radici,[5] D. Tieger,[4] W. Turchinetz,[4] C. E. Vellidis,[8] L. Weinstein,[4,††] and S. Williamson[1]

[1]*Nuclear Physics Laboratory, University of Illinois at Urbana-Champaign, Illinois 61820*
[2]*Arizona State University, Tempe, Arizona 85287-1504*
[3]*Institut für Kernphysik, Johannes Gutenberg Universität, D-55099 Mainz, Germany*
[4]*Massachusetts Institute of Technology, Cambridge, Massachusetts 02139*
[5]*Università di Pavia, Dipartimento di Fisica Nucleare e Teorica, and Istituto Nazionale di Fisica Nucleare–Sezione di Pavia,
Pavia, Italy*
[6]*California State University, Los Angeles, California 90032*
[7]*University of Massachusetts at Amherst, Amherst, Massachusetts 01003*
[8]*National and Capodistrian University of Athens, Athens, Greece*

The first measurements of f'_{LT}, known as the fifth response function, have been made for the $^2\text{H}(\vec{e},e'p)$ and
$^{12}\text{C}(\vec{e},e'p)$ reactions. This response is directly related to the imaginary part of the interference between the
transverse and longitudinal nuclear electromagnetic currents. Its observation requires longitudinally polarized
electron beams and out-of-plane detection, the latter made possible by the newly developed out-of-plane
spectrometer system. The initial measurements were made by using a 560-MeV polarized electron beam and
quasielastic kinematics at $Q^2 = 3.3$ fm^{-2}. The development of the methodology for out-of-plane physics, and
the analysis of the data from the initial experiments are described in detail. The measured fifth response and the
related asymmetry in the coincidence cross section are in agreement, albeit with large statistical errors, with the
theoretical predictions. Future extensions of the out-of-plane program are also discussed.
[S0556-2813(99)02812-5]

PACS number(s): 25.30.Fj, 24.70.+s, 27.10.+h, 27.20.+n

I. INTRODUCTION

The electromagnetic structure of nuclei, as probed
through electron scattering and electron-induced reactions,
can be characterized by a set of response functions [1–4].
With the detection in coincidence of the scattered electron
and a particle ejected from the target nucleus, the unpolar-
ized cross section contains four response functions. Each of
these response functions is determined by different combina-
tions of the longitudinal and transverse components of the
nuclear electromagnetic current, and thus provides different
information on the relevant nuclear structure.

The development of polarized beams and targets, and co-
incidence probes involving novel detectors capable of out-of-
plane detection and recoil polarimetry, is enabling access to
hitherto unobserved response functions. In particular, with
unpolarized targets and polarized electron beams, a fifth re-
sponse function can be measured. Whereas one of the previ-
ous four response functions is directly related to the real part
of the interference between the longitudinal and transverse
nuclear current, the fifth response is related to the corre-
sponding imaginary part. It vanishes identically in the ab-
sence of final-state interactions.

To isolate the various (five) responses that arise in coin-
cidence scattering with polarized incident electrons, we have
advocated [5] the simultaneous use of several approximately
equal detectors positioned on a cone around the momentum
transfer vector. Ratios of the yields from these detectors pro-
vide reduced sensitivity to systematic errors relative to those
attainable from sequential measurements. Further improve-
ment can be obtained when the detectors are interchanged. A
$\pi/4$ periodicity in the selection of azimuthal angles, and
hence detection of secondary decay particles out of the
electron-scattering plane, maximizes the sensitivity of the
separation [5].

As a first step towards implementing a systematic pro-
gram of measurements of the response functions for nucleon
resonances and few-body nuclei, measurements were made
of the fifth response function for the $^{12}\text{C}(\vec{e},e'p)$ and
$^2\text{H}(\vec{e},e'p)$ reactions by using a protype detector of a system
of four out-of-plane spectrometers (OOPS) [6,7]. A longitu-
dinally polarized beam of 560-MeV electrons impinged upon

---

*Present address: Raytheon Missile Systems, Loc. TU, Bldg. 801,
M/S H15, 1151 E. Hermans Rd., Tucson, AZ 85734-1137.

†Present address: Institut für Kernphysik der Universität Mainz,
D-55099 Mainz, Germany.

‡Present address: University of Kentucky, Lexington, KY 40506.

§Present address: Schillerstr. 26, 78576 Emmingen, Germany.

∥Present address: TRIUMF, 4004 Westbrook Mall, Vancouver
BC, Canada V6T 2A3.

¶Present address: Kyungpook National University, Taegu 702-
701, S. Korea.

**Present address: Massachusetts General Hospital, Nuclear
Magnetic Resonance Center, Charlestown, MA 02129.

††Present address: Old Dominion University, Norfolk, VA 23529.
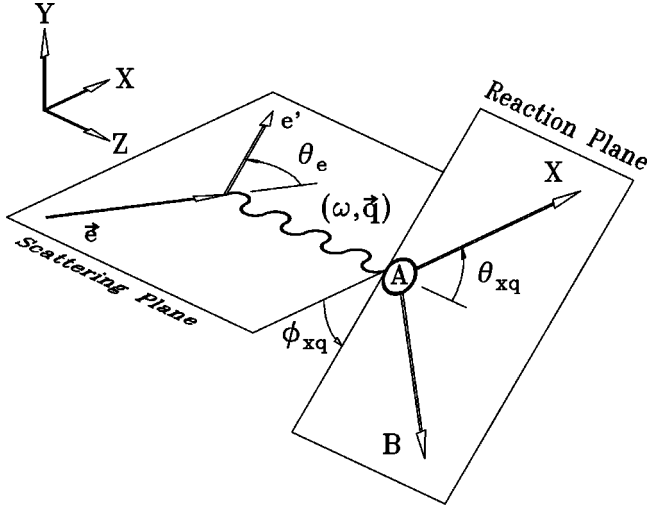
FIG. 1. Kinematic definitions for the $A(\vec{e},e'X)B$ reaction.

a solid carbon foil or a liquid deuterium target, and the scattered electrons were detected in coincidence with ejected protons in the OOPS. In these cases, the fifth response could be measured with little systematic error as an asymmetry between cross sections for oppositely signed incident electron polarizations. Data were obtained for two proton angles out of the electron scattering plane and directly above the momentum-transfer vector. The electron kinematics were set for quasielastic scattering at a momentum transfer of 1.8 fm^{-1} and held constant throughout the experiment.

Short reports on these experiments have been given elsewhere [8,9]. In this paper we present detailed descriptions of the methodology of out-of-plane measurements, our experimental apparatus and procedures, and the analysis of the data. Additional information on the theoretical calculations as applied to these data are also given, along with interpretations of the sensitivity of the fifth response to parameters in the models. Finally, some future prospects for additional measurements are discussed.

A. Kinematic variables and responses

Electron scattering in the one-photon-exchange approximation (OPEA) is illustrated in Fig. 1 with the electron and reaction planes shown for clarification. The target nucleus is indicated by A and the ejected particle X (also denoted x) is detected in coincidence with the scattered electron. The recoiling system B may or may not be in its ground state. An electron of energy E_i scatters through an angle θ_e to a final energy E_f. The electron transfers energy ω and momentum $\vec{q}$ to the nucleus. Because the electron vertex is kinematically determined and the momentum four-vector of the decay particle is measured, the missing momentum and energy of the residual system can be inferred. The missing momentum $\vec{p}_m$ is simply

$$\vec{p}_m \equiv \vec{q} - \vec{p}_x, \tag{1}$$

where $\vec{p}_x$ is the momentum of the ''x'' particle. The missing

energy E_m is defined as the binding energy (E_b) of the ejected particle to B plus the internal excitation energy (E_{ex}) of the residual nucleus. Thus

$$E_m \equiv M_B^* + M_x - M_A \quad (=E_b + E_{ex})$$
$$= \omega - T_x - T_B, \tag{2}$$

where T_x is the kinetic energy of x, T_B is that of the residual nucleus, and M_B^* is equal to the ground-state mass of the residual nucleus plus the excitation energy.

The cross section for the scattering process depicted in Fig. 1 (OPEA) can be calculated from the matrix elements of the electron and nuclear currents $j^{\mu'}$ and J_{fi}^μ. We take the squared four-momentum transfer $Q^2 > 0$. In the absence of detected initial or final hadronic-state polarization, the cross section for polarized electron scattering in the laboratory may be expressed as [4]

$$\frac{d^5\sigma}{d\omega\, d\Omega_e\, d\Omega_x} = K\sigma_{\text{Mott}}\{v_L f_L + v_T f_T + v_{TT} f_{TT}\cos 2\phi_{xq}$$
$$+ v_{LT} f_{LT}\cos\phi_{xq} + h P_B v'_{LT} f'_{LT}\sin\phi_{xq}\}, \tag{3}$$

with

$$K = |\vec{p}_x| E_x \left(1 - \frac{E_x}{E_B}\frac{\vec{p}'\cdot\vec{p}_m}{\vec{p}'^2}\right)^{-1}. \tag{4}$$

In this equation, K includes a phase-space and a recoil factor, σ_{Mott} is the cross section for elastic Coulomb scattering from an infinitely massive point target (including a factor for the charge of the target), ϕ_{xq} is the azimuthal angle of the decay product in a spherical coordinate system about the momentum transfer vector, as shown in Fig. 1, h is the helicity of the electron beam ($h = \pm 1$), and P_B is the magnitude of the beam polarization. The subscripts L and T refer to longitudinal and transverse components, respectively, with double subscripts indicating interference terms. The v_i ($i = L,T,LT$, or TT) and v'_{LT} are obtained from the electron current and are simple functions of electron kinematical variables. The responses f_i and f'_{LT} are proportional to bilinear combinations of the nuclear current matrix elements and contain all of the nuclear structure information. The responses in general depend on the polar opening angle θ_{xq}, the momentum p_x of the decay particle, and the values of ω and $\vec{q}$. Detection of the fifth response f'_{LT} requires both polarized electrons and the detection of secondary particles out of the electron scattering plane. Further details may be found in Refs. [1–4].

By measuring cross sections at several values of ϕ_{xq} on a cone of constant θ_{xq} with fixed electron kinematics, the interference responses can be isolated. If the transverse and longitudinal responses are combined into a single direct term as $f_d = v_L f_L + v_T f_T$, one can separate the responses in terms of cross section differences ($D_{\phi_1,\phi_2} \equiv \sigma(\phi_1) - \sigma(\phi_2)$) and sums ($S_{\phi_1,\phi_2} \equiv \sigma(\phi_1) + \sigma(\phi_2)$). Thus,

$$f_{LT} = \frac{D_{0,\pi}}{2K\sigma_{\mathrm{Mott}}v_{LT}}, \tag{5}$$

$$f'_{LT} = \frac{D_{\pi/2,3\pi/2}}{2K\sigma_{\mathrm{Mott}}P_B v'_{LT}},$$

$$f_{TT} = \frac{S_{0,\pi} - S_{\pi/2,3\pi/2}}{4K\sigma_{\mathrm{Mott}}v_{TT}},$$

$$f_d = \frac{S_{0,\pi} + S_{\pi/2,3\pi/2}}{4K\sigma_{\mathrm{Mott}}}.$$

By combining out-of-plane particle detection with a Rosenbluth separation, in which the direct term f_d is separated into f_L and f_T by varying the electron kinematics, all five responses can be identified. Equations (5) suggest the great value of the simultaneous cross section measurements with four detectors. Systematic errors can be minimized by the use of the ratios of yields. The single spectrometer employed in the experiments reported here was the prototype module for the four-OOPS system, built specifically to exploit the above relationships.

Equation (3) can be rewritten to emphasize the helicity dependent term [2]:

$$\frac{d^5\sigma}{d\omega\,d\Omega_e d\Omega_x} = \Sigma + hP_B\Delta. \tag{6}$$

Here Σ is the cross section that is measured with an unpolarized beam, and Δ can be extracted when the initial electrons are longitudinally polarized.

The contribution of Δ to the full cross section can be measured with very little systematic error in the form of an asymmetry corresponding to the analyzing power of the electron beam. This electron-beam asymmetry between cross sections measured in a single detector for each sign of the beam polarization is

$$A_e = \frac{d\sigma_+ - d\sigma_-}{d\sigma_+ + d\sigma_-} = \frac{P_B\Delta}{\Sigma}. \tag{7}$$

Because we consider $(e,e'p)$ reactions exclusively in this work, the particle X is hereafter identified with the proton p.

B. Fifth response in quasifree $(e,e'p)$ scattering from ^{12}C and ^{2}H

The fifth response is determined from the asymmetry and an absolute measurement of the unpolarized cross section,

$$f'_{LT} = \frac{A_e\Sigma}{K\sigma_{\mathrm{Mott}}P_B v'_{LT}\sin\phi_{xq}}. \tag{8}$$

Because f'_{LT} is the imaginary part of the interference between the longitudinal and transverse (LT) components of the nuclear current (the contraction of the antisymmetric parts of the lepton and hadron tensors), it vanishes in the absence of final-state interactions or when a single phase

dominates all projections of the current $J^\mu_{fi} = |J^\mu_{fi}|e^{i\delta}$, for then the LT product is purely real. For multiple reaction channels which add coherently, f'_{LT} may be nonzero. The fifth response thus provides a means of measuring the contributions from small ''background'' channels which are often too weak to be observed directly in total cross section measurements. One example is the relative sensitivities of the different response functions f_i and f'_{LT} in the $N\to\Delta$ transition to resonant quadrupole-excitation terms and nonresonant Born terms [5]. Similarly, in quasielastic knock-out kinematics on nuclei of atomic mass greater than one, the dominant amplitude is that of the direct knockout process. Weaker amplitudes, such as those of rescattering and in some instances those of meson exchange-current contributions, are revealed through their interference with the dominant amplitude. It is therefore not surprising that in such cases f'_{LT} is highly sensitive to final-state interactions and vanishes [10,11] in the plane-wave impulse approximation (PWIA), where rescattering is ignored. The fifth response in ^{12}C and ^{2}H investigated in the present work are examples of this latter category.

The phenomenological treatment of final-state interactions makes it difficult to study several interesting nuclear phenomena which require precise analysis of the reaction beyond the impulse approximation. For instance, such precision is required when the coupling of the virtual photon to a virtual meson or to a correlated pair of nucleons needs to be properly considered. Single-arm electron scattering cross sections on ^{2}H, ^{3}H, and ^{3}He are well described by calculations only after the inclusion of meson exchange currents (MEC) and isobar configurations (IC) [12]. Similarly, the size of the contributions of MEC and IC to the separate responses of the ^{16}O$(e,e'p)$ reaction have been calculated [13]. In the latter case, two-body currents are found to have a pronounced effect ($\approx 25\%$) on the transverse (f_T) and transverse-transverse interference (f_{TT}) terms. However, the same calculations also show that uncertainties introduced by differences between optical potentials in distorted-wave impulse-approximation (DWIA) calculations of the cross section are nearly as large.

In quasielastic knock-out kinematics, the fifth response offers an observable that is particularly sensitive to the effects mentioned above, and it can thus help to understand them. Calculations indicate that f'_{LT} is primarily sensitive to the interference between the direct PWIA and rescattering amplitudes. Moreover, this new observable can be measured with extreme accuracy due to the insensitivity to systematic error which is inherent in measurements of helicity asymmetries. It can constrain DWIA optical model calculations and help guide theories that attempt a consistent treatment of the direct and rescattering amplitudes beyond the mean-field approach.

In the momentum-transfer region explored by our experiment along the quasielastic ridge, theoretical calculations [14–16] indicate that meson exchange currents (MEC), isobar configurations (IC), and final-state interactions (FSI) are minimized. All three effects become important when straying from quasielastic kinematics. The effects of IC become important above the quasielastic ridge at low momentum

TABLE I. Beam parameters.

Energy	560 ± 1.5 MeV
Energy spread	0.2% full width at half maximum
Tune	Recirculated, achromatic
Rep. rate	580 Hz
Pulse width	11 μs
Duty factor	0.64%
Polarization	34.2% ± 3.2%
Peak current	≤157 μA
Average current	0.8 μA

TABLE II. Kinematics for the electron vertex (E_i = 560 MeV). These quantities are given for the central values of the electron spectrometer.

E_f	490.8 MeV
ω	69.2 MeV
Q^2	3.31 fm^{-2}
$|\vec{q}|$	1.85 fm^{-1}
θ_e	40.0°
θ_q	59.8°
$\Delta\omega$	16.8 MeV
$\Delta\Omega$	4.99 msr

transfer and high-energy transfer, while those from MEC become important below the quasielastic ridge at high momentum transfer and low-energy transfer. In all kinematics, f'_{LT} appears to be sensitive to rescattering. Moreover, f_{LT} is sensitive to the *NN* potential in certain kinematic regions, and f_{TT} is sensitive to IC in certain kinematic regions and is sensitive to MEC at threshold.

In our measurements of ^{12}C($\vec{e},e'p$) and ^{2}H($\vec{e},e'p$), the two dominant amplitudes that interfere, giving rise to f'_{LT}, are the ones due to the direct (PWIA) knock-out and rescattering processes. Thus our experiment is well suited to test the treatment of final-state interactions. The fifth response f'_{LT} has never been previously measured, due to difficulties associated with the out-of-plane detection of the proton and the lack of polarized beams.

II. EXPERIMENTAL METHOD

The ^{12}C($\vec{e},e'p$) and ^{2}H($\vec{e},e'p$) measurements were performed in the North Experimental Hall at the Bates Linear Accelerator Center, and measurements of the beam polarization with a Møller polarimeter were performed in the South Experimental Hall. Several key parameters of the beam employed in our measurements are listed in Table I. At the time of the experiment, due to the lack of a spin manipulation system, maximally polarized beams could be delivered only at energies specific to each experimental hall. The same longitudinal polarization in each hall could be provided with a compromise beam energy of 558 MeV. This polarization was 98% of the maximum polarization expected from the polarized electron source.

Longitudinally polarized electrons were produced by the photoemission of electrons from a gallium-arsenide (GaAs) crystal with circularly polarized laser light. The source had the capability of rapid helicity reversal without the introduction of helicity-correlated effects. The laser system consisted of a two-Watt krypton-ion laser and several optical elements to create circularly polarized light modulated to the duty factor of the accelerator. The helicity of the beam was flipped randomly on a pulse-by-pulse basis to minimize the introduction of helicity-correlated effects.

The energy loss spectrometer system (ELSSY) [17] was used to detect electrons and was set at a scattering angle of 40°. Kinematic quantities for the electron are given in Table II. The missing energies were E_m = 2.2 MeV for ^{2}H and 15 MeV < E_m < 28 MeV for ^{12}C, the latter corresponding to knockout of a *p*-shell proton. Statistically significant results could not be obtained for the *s*-shell portion of the missing-energy spectrum from ^{12}C.

A single OOPS module [6,7] with a solid angle of 1.2 msr was used as the out-of-plane proton spectrometer. It was set along the central momentum-transfer axis at an angle of 59.6° with respect to the beam. The kinematic parameters of the proton arm and unobserved residual particle *B* are given in Table III. In this table p_p^{Lab} (p_B^{Lab}) and T_p^{Lab} (T_B^{Lab}) represent the laboratory momentum and kinetic energy of the proton (residual nucleus), respectively. The out-of-plane angles were achieved by placing the spectrometer directly above the momentum transfer axis (ϕ_{pq} = 90°) at θ_{pq} angles of 0°, 20.9° (denoted as 21°), and 29°. The in-plane point provided a check on systematic errors by measuring a null asymmetry. The other angles were determined from both physics and mechanical constraints.

TABLE III. Kinematics for the proton arm (E_i = 560 MeV). The center-of-mass (c.m.) angle is in the recoiling hadronic system.

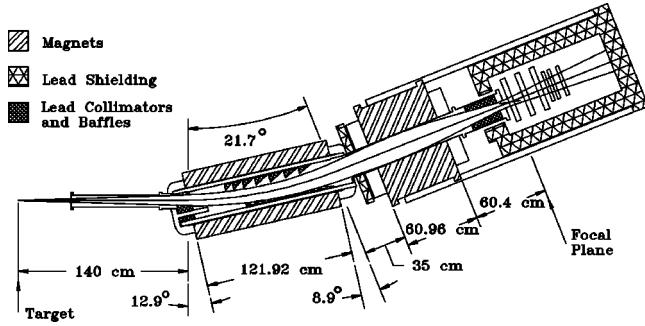| θ_{pq}^{Lab}(deg)	$\theta_{pq}^{\text{c.m.}}$ (deg)	p_p^{Lab} (MeV/c)	T_p^{Lab} (MeV)	θ_{Bq}^{Lab} (deg)	p_B^{Lab} (MeV/c)	T_B^{Lab} (MeV)
^{2}H						
0	0.0	359.4	66.4	0.0	6.2	0.0
20.9	43.3	333.3	57.4	−65.5	130.7	9.1
29	60.0	309.9	49.8	−57.8	177.5	16.6
^{12}C						
20.9	23.2	316.4	51.9	−58.1	132.9	0.9
29	32.1	314.3	51.2	−59.2	177.3	1.5

FIG. 2. An elevation view of an OOPS module in cross section. The key elements of the spectrometer are drawn to scale.

The spectrometer is a dipole-quadrupole design. An elevation view of the spectrometer is given in Fig. 2. The dipole magnet in the spectrometer disperses particles through a 21.7° bend with a 3.47-m bend radius. The detector system is enclosed in a lead compartment at the rear of the spectrometer. The compartment is composed of 15-cm-thick lead walls and is supported by a 5-cm-thick steel octagonal tube. The tube supports not only the lead shielding for the detectors, but also the quadrupole magnet and ultimately the entire weight of the spectrometer.

The focal plane is tilted at an angle of 12.7° to the central ray and its dispersion is 0.22 cm/%. The OOPS detector system was composed of three horizontal drift chambers (HDC) and three scintillators. A six-fold coincidence is formed among the scintillator signals to generate the OOPS trigger and also the timing reference for the HDC's.

A 5.08-cm liquid deuterium target was used for the ^{2}H$(\vec{e},e'p)$ measurements. The liquid was held in an elgiloy [18] container that was 5.08 cm in diameter and had a combined wall thickness of 84.3 mg/cm^2. Some important parameters of the target can be found in Table IV. The refrigeration system was designed to provide a maximum of 50 Watts of cooling power to the target. The temperature of the target was measured by a carbon glass resistor with an accuracy of 0.5 K, built into the bottom of the target cell.

The refrigeration system could not keep liquid in the target when ≥ 1 μA of beam was put on target. The 21° data were taken with ^{2}H lying mostly along the phase boundary between liquid and gas. The 29° data were obtained with the target in the liquid region of the phase diagram, but most of the data are near the phase boundary. In these cases the target was not in a state of equilibrium, so the target thickness is not known. This uncertainty made the extraction of absolute cross sections difficult, but was not a significant source of concern for the asymmetry measurements.

To eliminate background from reactions occurring in the walls of the cryogenic cell, Kennertium [19] blocks 2.54-cm square by 7.62-cm tall were placed close to the target. In this configuration the OOPS viewed approximately 2.54 cm of the target and ELSSY viewed the full 5.08-cm length. In studies with an empty target cell, no coincidences were observed.

Two flat foils of natural carbon of thicknesses 200 and 600 mg/cm^2 were used for the carbon targets. About half of the data at $\theta_{pq}=21°$ were obtained with the thick target, the remainder of the data with the thin target. The degradation in energy resolution with the thick target was not a significant problem for the asymmetry measurement.

III. ANALYSIS

The data-reduction process requires many steps and techniques, including an extensive Monte Carlo simulation. The following procedure was followed:

(1) Calibration of wire chambers and determination of detection efficiencies for each spectrometer. Raw wire chamber information was converted to distances in the focal-plane region which were ultimately used to calculate the kinematic parameters of the scattered electron and the ejected protons at the target.

(2) Determination of the beam energy and polarization.

(3) Determination of the total charge and the charge for each helicity.

(4) Elimination of spurious events through kinematic restrictions and temporal correlations.

(5) Correction of the time-of-flight (TOF) spectra for various effects in order to reduce accidental coincidences.

(6) Determination of the missing energy for kinematically corrected coincidences.

(7) Generation of TOF spectra constrained by cuts on missing energy spectra.

(8) Determination of the electron beam asymmetry [Eq. (7)] through helicity-tagged TOF spectra.

(9) Determination of the coincidence cross section. To do so, it is necessary to correct for spectrometer acceptance efficiencies, correct for radiative effects, and correct for target effects.

(10) Calculation of the fifth response by normalizing to the electron beam asymmetry, Eq. (8).

Details of these procedures are presented in this section.

A. ELSSY detector system

The ELSSY detector system was composed of two vertical drift chambers (VDC), two transverse arrays (TA), two

TABLE IV. Target cell parameters.

	Target	Walls
Material	Liquid deuterium	Elgiloy (Co-Ni alloy)
Thickness	823 mg/cm^2 (5.08 cm)	84.4 mg/cm^2 (0.01 cm)
Density	0.162 gm/cm^3	8.3 gm/cm^3
Radiation length	757 cm	$\approx$ 1.76 cm

scintillators, and one Čerenkov detector. It enabled the determination of the electron trajectories at the target. The measurements of the absolute cross sections required that detection efficiencies be measured as well. The two ELSSY vertical drift chambers were used to measure focal-plane positions and angles along the dispersive direction [20–22]. The signal wires were bused together on three separate delay lines. A time-to-amplitude converter (TDC) was connected to each end of each delay line. The TDC start was formed from scintillators in the ELSSY trigger and the TDC stop was determined from signals on the delay line.

The drift time was converted to a distance by using an experimentally determined lookup table. To measure positions and angles, the VDC was oriented along the focal plane, which is at 45° with respect to the central ray. The position and angle resolutions of the individual VDC's are ≈ 140 μm and ≈ 17 mr, respectively [20]. By using the position information from the chambers, the angular resolution was improved to ≈ 2.8 mr.

The VDC efficiencies were calculated by using events with trajectories that would intersect all of the detectors. The active areas of the VDC's do not completely overlap one another or the trigger detectors. The ELSSY trigger requires that the two scintillators and the Čerenkov detector present a coincidence event. For all of our measurements the VDC efficiency (ϵ_{VDC}) was constant at 0.935 ± 0.005.

The two ELSSY transverse arrays were used to measure focal-plane positions and angles perpendicular to the dispersive direction. Each TA was composed of two HDC wire planes, which were composed of alternating signal ($\phi 20$ μm) and field-shaping wires (ϕ 20 μm). The field-shaping wires were at positive high voltage and the signal wires were at negative high voltage. The signal wires were ganged together on a single delay line. A TDC was connected to each end of the delay line. As with the VDC, the wire that had been hit could be determined from the difference in the times that it took the signal to reach the ends of the delay line. This drift time was converted to a distance by using an experimentally determined lookup table.

The left-right ambiguity characteristic of such chambers was removed by the use of the second HDC in each TA chamber. The signal wires of the second HDC were offset from the first HDC by 1/2 of a signal wire spacing. The TA chambers in ELSSY were mounted perpendicular to the central ray in the transverse plane. The position resolution of the individual TA chambers was ≈ 140 μm [23]. The combined angular resolution of the combined TA chambers was ≈ 1 mr [23]. The TA detector efficiency (ϵ_{TA}) during the course of our measurements was approximately constant, ranging in values of between 0.92 to 0.94.

The efficiency for the ELSSY spectrometer is the combination of all the subsystem efficiencies and those events that may have corrupt wire chamber TDC times. It takes a maximum of ≈ 300 ns for the ions in the drift chamber to reach the signal wire. Events that occur within this time period may have TDC times that have been corrupted by other events that occur within the same time period. The corrupted events within the time period are separately counted. The efficiency for detecting good events in ELSSY is

$$\epsilon_{ELSSY} = \epsilon_{VDC}\epsilon_{TA}\epsilon_{trigger}\left(1 - \frac{N_{TDC\text{-}corrupt}}{N_{raw}}\right), \quad (9)$$

where $N_{TDC\text{-}corrupt}$ is the total number of corrupt wire chamber TDC events and N_{raw} is the total number of events counted. The detection efficiency of the ELSSY trigger detectors was determined to be 1.00 ± 0.02, based on (e,e') cross section measurements from ^{12}C and ^{16}O [24].

B. OOPS detector system

The OOPS detector system was composed of three HDC's and three scintillators. As was stated earlier, only good position and angular measurements of proton trajectories from the detector system are needed for the asymmetry measurement and for the determination of the target variables. In order to determine absolute cross sections, detection efficiencies were also needed.

Three horizontal drift chambers were used to measure focal-plane X and Y positions, and θ and ϕ angles. Each chamber contained two orthogonal HDC wire planes. A detailed explanation of the operation of the OOPS HDC can be found in Refs. [25–27]. Each HDC plane was composed of alternating guard (ϕ 76 μm) and signal (ϕ 20 μm) wires. The guard wires were grounded and the signal wires were at positive high voltage (2600 V). The wires were sandwiched between two sets of aluminized mylar windows, which were grounded. The field lines, for the most part, ran horizontally from guard wire to signal wire. A gas mixture of 65% argon, 35% isobutane, and 0.5% alcohol was used in the HDCs [25,28]. The signal wires were ganged together on a single delay line. Alternating guard wires were ganged together on two separate bus lines. A TDC was connected to each end of the delay line. The wire that had been hit could be determined from the difference in the times that it took the signal to reach the ends of the delay line. The time sums of the delay line ends indicated the total time it took the ions to drift to the signal wire. This drift time was converted to a distance by using an experimentally determined lookup table.

Once the hit wire had been identified and the distance from the wire was known, an ambiguity remained as to which side of the wire had been hit. This ambiguity was removed by using the guard wires. The HDC's in the OOPS were mounted perpendicular to the central ray in both the dispersive and transverse planes. A single HDC chamber allows for the measurement of the X and Y positions. The use of a second HDC chamber allowed for the measurement of the θ and ϕ angles. The position resolution of each HDC was 174 ± 9 μm [25,28]. The chambers were placed ≈ 12.1 cm apart in the detector package. This arrangement resulted in an angular resolution of 1.44 ± 0.07 mr.

Information from all three chambers and the scintillators was used to determine the HDC detection efficiency. Two of the three chambers in both X and Y must fire in order to determine trajectory position and angle. Positions from two chambers were a necessary but not a sufficient condition for proper determination of trajectory position and angle. Additional tests were placed on the wire chamber information in
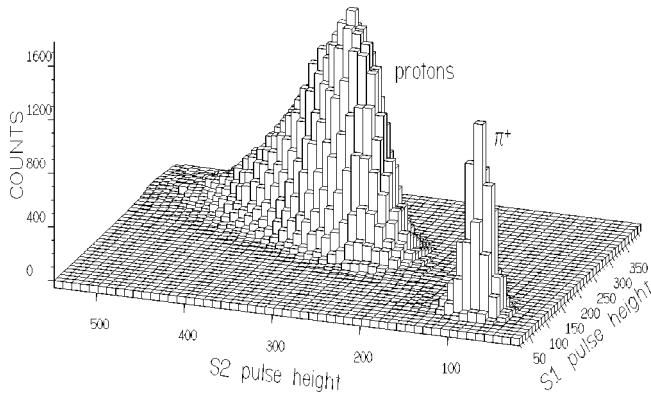
FIG. 3. The pulse-height distributions for OOPS scintillators 1 and 2. Pions and protons are easily differentiated.

order to determine a good trajectory. The efficiency of determining good trajectories was determined from the ratio of good trajectory events to all raw wire chamber events. The total HDC efficiency for our measurements was found to be $\epsilon_{HDC} = 0.89 \pm 0.01$.

The efficiency of the OOPS module is the combination of all the subsystem efficiencies as well as corrupt wire chamber TDC events. The efficiency for detecting good events in OOPS is

$$\epsilon_{OOPS} = \epsilon_{HDC}\epsilon_{trigger}\left(1 - \frac{N_{TDC\text{-}corrupt}}{N_{raw}}\right). \qquad (10)$$

The trigger efficiency was not 100% due to the electronics configuration. Scalers were placed throughout the OOPS trigger network so that event rates could be calculated. The calculation of the trigger efficiency is discussed in Ref. [24]. The total OOPS efficiency was found to be 0.85 ± 0.01 during the course of our measurements.

C. Particle identification

In our measurements pions that could have been misidentified either as electrons or protons were of concern in both the OOPS and ELSSY spectrometers. Special detectors were implemented in the spectrometers to eliminate the unwanted particles.

A Čerenkov detector filled with isobutane gas at atmospheric pressure was used in ELSSY to identify electrons. Slow moving pions could not fire the Čerenkov and thus did not register as an event.

Protons in OOPS could be identified in any of the scintillator pulse-height histograms. Shown in Fig. 3 are the proton and pion peaks observed in the 0° data of scintillators 1 and 2. The separation between the protons and pions is very good with just one scintillator, and the pulse heights from scintillator 2 were used to identify the protons. The peak separation improves for the out-of-plane angles due to the lower-energy protons. Heavier particles such as deuterons lose too much energy in the scintillators and are stopped by the first two layers, never forming a trigger.
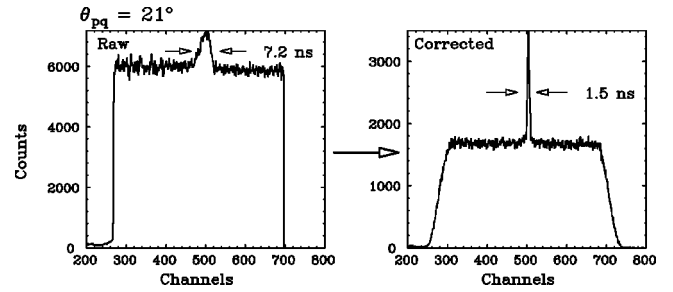

FIG. 4. Time-of-flight corrections for the 20.9° out-of-plane angle.

D. Time-of-flight corrections

A coincidence event was identified by the relative time that the reactant particles reach the trigger detector of each spectrometer. A timing window of 100 ns was set in hardware to identify a raw coincidence event. The observed timing peak was broadened by the following effects: (1) path lengths through the spectrometers vary due to finite acceptances; (2) particle speeds in the spectrometers differ due to different momenta; (3) the interaction points in trigger scintillators can vary; (4) the discriminators have time walk due to scintillator pulse heights; and (5) intrinsic electronic noise and instabilities in the counting chain. Corrections were applied to reduce the accidental background and to increase the signal-to-noise ratio. Items 1–3 could be corrected in software. Item 4 was corrected by the use of constant-fraction discriminators in hardware. Item 5 refers primarily to a delay-line instability problem in ELSSY, which was corrected in software for the 0° point.

The OOPS module had a momentum bite of approximately 10%, which contributed considerably to the time-of-flight peak broadening. Given the path length and the speed of the protons, the time correction was easily calculated. The proton path length was calculated from the measured focal plane coordinates of the event and the spectrometer matrix elements.

In ELSSY the dominant TOF correction comes from electron flight paths arising from θ_{target}. Electrons arriving at the focal plane have $\beta \approx 1$ so there are no speed variations to worry about. Path lengths were calculated from focal-plane variables and spectrometer matrix elements. After correcting for the above effects, the TOF peak had a width of ≈ 1.5 ns. The striking improvement between the raw and corrected TOF peaks for the 21° out-of-plane measurement are shown in Fig. 4.

E. Beam energy determination

An accurate determination of the beam energy was necessary for a reliable missing-energy calibration and estimates of systematic errors. Data acquisition was interrupted twice by major shut downs of the accelerator. After each shutdown a new beam energy calibration was performed. The standard method used to determine the beam energy off-line is the differential recoil method. This method and its variations are discussed in detail in Refs. [29] and [30]. The beam energies determined for each out-of-plane angle are given in Table V.

TABLE V. Beam energy for each out-of-plane angle measurement.

θ_{pq}	Beam momentum (MeV/c)
0°	561.5 ± 1.5
20.9°	561.5 ± 1.5
29°	559.5 ± 1.5

F. Missing energy determination and resolution

The missing energy defined by Eq. (2) was determined from measured kinematic quantities in the experiment. In doing so, it was necessary to account for the relatively large number of accidental events, as can be seen in the time-of-flight histograms of Fig. 4. Three cuts were placed on the time-of-flight histogram, one centered about the TOF peak at approximately the 3σ point, and two other cuts placed on either side of the reals peak in the ''flat'' region of the accidentals. The missing-energy accidentals spectrum was scaled by the ratio of the TOF-cut window widths and subtracted from the missing-energy reals spectrum to form the missing-energy trues spectrum. This sequence of events is illustrated in Fig. 5.

The bin size for the missing-energy histograms was chosen to be approximately equal to the experimental missing-energy resolution. If the small recoil kinetic energy of ^{11}B is
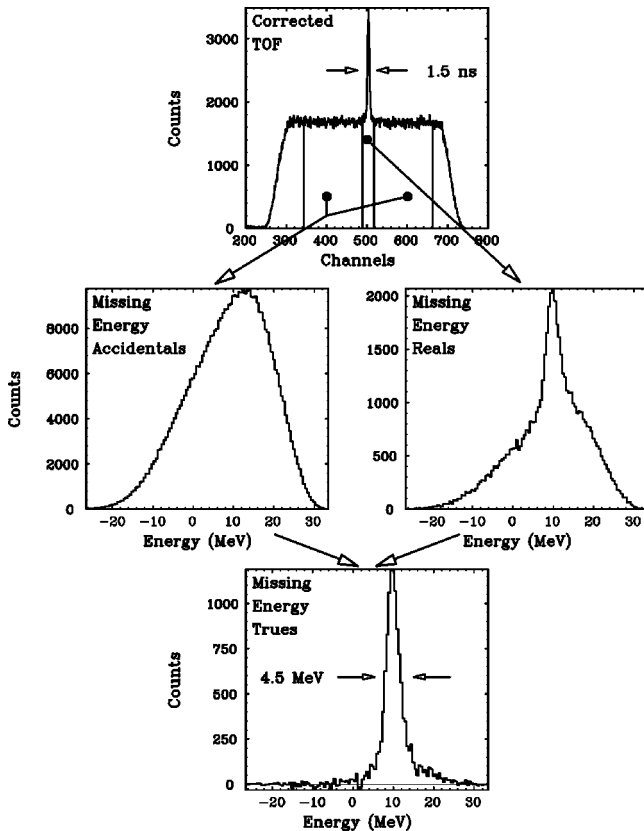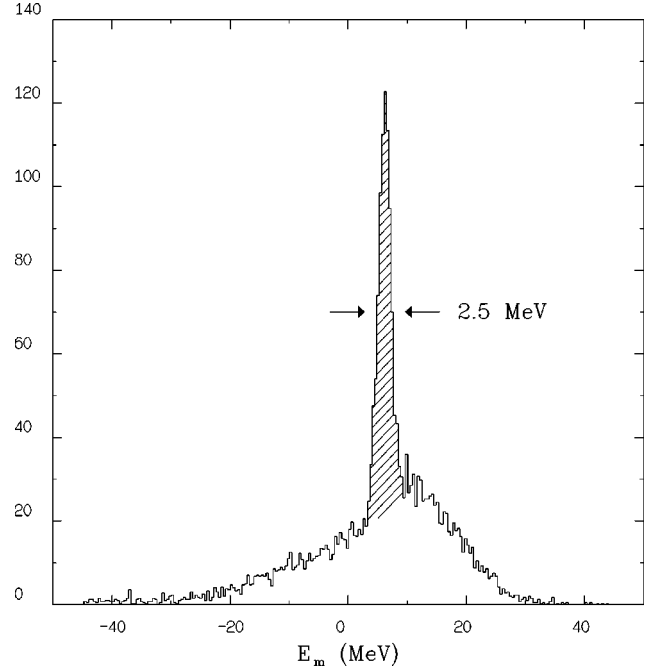

FIG. 6. The deuterium missing-energy spectrum without a TOF cut for a single run in parallel kinematics.

ignored, then the minimum missing-energy resolution is estimated to be

$$\delta E_m = \sqrt{(\delta\omega)^2 + (\delta T_p)^2} \approx \sqrt{(1.1 \text{ MeV})^2 + (0.9 \text{ MeV})^2}$$
$$\approx 1.5 \text{ MeV}. \tag{11}$$

The beam-energy spread and the OOPS resolution contribute about equally to the missing-energy resolution.

The missing energy of the peak in Fig. 5 is not at the value 2.2 MeV expected for deuterium. The shift arises predominantly from energy losses in the target, possibly with other shifts due to the uncertainty in beam energy. The shifts for deuterium were estimated from the experimentally determined effective target thicknesses (see Sec. III J 2) to be between 5–7 MeV, depending on the angle. The energy shifts for carbon ranged up to about 5 MeV.

A missing-energy spectrum without any TOF cuts for the ^{2}H($\vec{e},e'p$) reaction in parallel kinematics (0°) is shown in Fig. 6. The deuterium cross section and the trues-to-accidentals ratio are both large at these kinematics. The peak, which is cross-hatched and dotted in the figure, corresponds to correlated coincident events from the breakup of deuterium. The dotted area below the peak results from coincidences between uncorrelated electrons and protons. The shape of the accidentals spectrum is understood fairly well through a Monte Carlo calculation of the coincidence detection volume [24,31].

The resolution of the deuterium spectrum for a single run in Fig. 6 is about 2.5 MeV. The position and the width of the deuterium peak are consistent with the results of our Monte Carlo code AEEXB [31]. The increase above the estimated resolution can be attributed to effects from the energy loss and multiple scattering of the protons in the target, and also
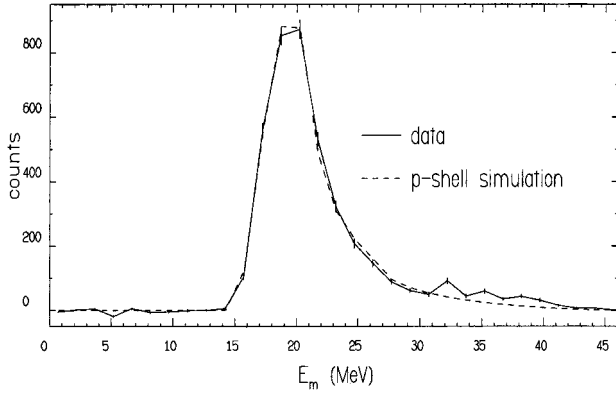

FIG. 5. ''Cuts'' on a ^{2}H($\vec{e},e'p$) time-of-flight spectrum for $\theta_{pq}=20.9°$, which generate the ''accidentals,'' ''reals,'' and ''trues'' missing-energy spectra.

FIG. 7. The measured ^{12}C missing-energy spectrum at $\theta_{pq}=20.9°$ compared with a Monte Carlo simulation.

the angle and momentum resolutions of both spectrometers. When events are summed for multiple runs, however, the width of the peak increased to about 3.6–5.0 MeV, depending on the angle. This broadening is attributed primarily to density fluctuations in the liquid target [31].

For ^{12}C a comparison of a measured spectrum to our Monte Carlo simulation is shown in Fig. 7. In addition to the ^{11}B ground state, the simulation includes two excited states at 2.1 and 5.0 MeV according to the experimental ratios measured at NIKHEF [32]. The shape of the missing-energy spectrum is accurately reproduced by the simulation. The normalization for the simulation was chosen to produce zero integrated strength in the difference between the simulation and the data from 14 to 28 MeV.

G. Charge determination

Two toroids were used to monitor the beam current and thus the charge accumulated during the measurement. This method has an absolute accuracy of better than 0.1% [33]. The second toroid was used in combination with an analog-to-digital converter to determine the charge accumulated on a pulse by pulse basis. Because each beam pulse had a helicity tag, the total charge accumulated for each helicity could be determined.

The total accumulated charge, the charge accumulated for each helicity, and the asymmetry in the helicity-dependent charge for the measurements are given in Table VI. Data were accumulated for a period of 5.8, 61.0, and 83.1 h for the $0°$, $21°$, and $29°$ ^{2}H$(\vec{e},e'p)$ points, respectively. The average current was approximately 0.8 μA. Data were accumulated for a period of 32 h for both the $21°$ and $29°$ ^{12}C$(\vec{e},e'p)$ points.

H. Polarization determination

The Bates Møller polarimeter located in the South Experimental Hall [34] was used to determine the longitudinal polarization of the beam. The measurements were performed once during the $0°$ (in-plane) runs, at the beginning of the $21°$ runs, and finally between the $21°$ and $29°$ runs. The most accurate data were taken during the second and third measurements.

The beam polarization was determined by measuring the asymmetry in the number of counts in a given detector as the beam helicity is flipped,

$$A_P = \frac{N_+ - N_-}{N_+ + N_-}. \tag{12}$$

If the helicity-correlated counts $N_\pm$ are normalized to the integrated beam current, then the beam polarization in the absence of background is given by

$$P_B = \frac{A_P}{P_T A_{zz} F(\theta_s)}, \tag{13}$$

where

$$F(\theta_s) = \cos\theta_s \cos\theta_T \left[1 + \frac{A_{xx}}{A_{zz}} \tan\theta_s \tan\theta_T \cos\phi_s \cos\phi_T \right]. \tag{14}$$

The variables θ_s and ϕ_s (θ_T and ϕ_T) are spherical angles of the electron (target) spin about the beam, and P_T is the target polarization. The definitions of A_{ii} are

$$A_{zz} = -\frac{(7+\cos^2\theta_{c.m.})\sin^2\theta_{c.m.}}{(3+\cos^2\theta_{c.m.})^2}, \tag{15}$$

$$-A_{xx} = A_{yy} = \frac{\sin^4\theta_{c.m.}}{(3+\cos^2\theta_{c.m.})^2}. \tag{16}$$

The center-of-mass scattering angle is $\theta_{c.m.}$. At $\theta_{c.m.}=90°$, the asymmetries A_{xx}, A_{yy}, and A_{zz} are maximized. The polarimeter was set up such that the asymmetries were maximized.

The measured asymmetry is diluted by background processes (other than Møller scattering), thus

$$A_P = A_{meas}(1+1/(S/N)), \tag{17}$$

TABLE VI. Charge accumulated during the ^{2}H and ^{12}C measurements for each out-of-plane angle.

θ_{pq}	^{2}H		^{12}C	
	Total charge (C)	Asymmetry	Total charge (C)	Asymmetry
$0°$	1.57×10^{-2}	-8.83×10^{-4}		
$20.9°$	0.19	5.42×10^{-4}	0.108	$+1.8\times10^{-3}$
$29°$	0.23	-0.11×10^{-2}	0.131,0.118	-1.2×10^{-3}

TABLE VII. The measured electron beam asymmetries A_e and the full values A corrected for beam polarization.

θ_{pq}	^{2}H		^{12}C	
	$A_e \times 10^2$	$A \times 10^2$	$A_e \times 10^2$	$A \times 10^2$
0°	$+0.64 \pm 0.34$	1.87 ± 0.99		
20.9°	-1.05 ± 1.18	-3.07 ± 3.45	$+3.31 \pm 1.48$	$+9.74 \pm 4.46$
29°	-4.72 ± 3.75	-13.80 ± 10.97	-1.08 ± 1.60	-3.18 ± 4.72

where A_{meas} is the measured asymmetry and S/N is the signal-to-noise ratio. In our experiment S/N was found to be 1.1 ± 0.08 at the peak.

Statistical errors of 0.6% for the measurements of polarization were achieved. The deviation between the two detectors of the polarimeter gives an estimate of the systematic error [34]. We take the polarization to be $34.2 \pm 0.2 \pm 3.2$, where the errors are statistical and systematic, respectively. Adding the statistical and systematic error in quadrature yields a relative error of 9.4%. This value is comparable to the 12% relative error determined during previous measurements of the beam polarization at Bates [34].

I. Asymmetry extraction

The measured electron beam asymmetry was formed from the true coincidence counts for each helicity by the expression

$$A_e = \frac{N_t^+ - N_t^-}{N_t^+ + N_t^-}. \tag{18}$$

The true counts were identified by the characteristic peak in the time-of-flight spectra. This peak sat on a flat background of accidentals which was subtracted to determine a meaningful asymmetry

$$N_t^\pm = N^\pm - A_t^\pm, \tag{19}$$

where $N^\pm$ is the total number of counts within the trues window for each helicity and $A_t^\pm$ is the total number of accidental counts within the trues window for each helicity. The total error in the asymmetry is

$$\delta A_e = \frac{1 - A_e^2}{2} \sqrt{\frac{1}{N_t^+}\left(1 + \frac{1 + R^+}{N_t^+/A_t^+}\right) + \frac{1}{N_t^-}\left(1 + \frac{1 + R^-}{N_t^-/A_t^-}\right)}, \tag{20}$$

where $R^\pm$ is the ratio of the trues-window width to the accidentals-window width for each helicity, and $N_t^\pm/A_t^\pm$ is the trues-to-accidentals ratio within the trues window for each helicity (N_t/A_t is also called the signal to noise ratio, S/N).

There were a comparatively large number of accidentals, especially at the out-of-plane angles. They were reduced substantially by placing a cut on the missing-energy spectra. The range of the accepted events was chosen such that it mini-

mized the error on the asymmetry. The asymmetries were determined from the helicity-tagged, cut, time-of-flight spectra.

For ^{12}C, a minimal requirement on the missing energy was the exclusion of s-shell events. The least discriminating test integrated over the p shell from the threshold at 16 MeV to the beginning of the s shell around 29 MeV. The cut was then narrowed in order to test for nonstatistical variations in the asymmetries and to attempt to reduce the error by increasing the ratio $N_t^\pm/A^\pm$ in Eq. (20). The asymmetry A_e and the error δA_e were then calculated for every possible symmetric window around the TOF peak.

The measured asymmetries must be scaled by the beam polarization to obtain the true asymmetries

$$A = \frac{A_e}{P_B}. \tag{21}$$

The beam polarization P_B was measured to be 0.34 within error bars of about 10%, as described in Sec. III H. The error on A is

$$\delta A = |A| \cdot \left\{ \left(\frac{\delta A_e}{A_e}\right)^2 + \left(\frac{\delta P_B}{P_B}\right)^2 \right\}^{1/2}. \tag{22}$$

Relative to the statistical errors of this measurement, the error produced by the uncertainty in the polarization is negligible. The resulting asymmetries are given in Table VII.

J. Absolute cross section

In addition to the effects considered so far, determination of the absolute coincidence ^{2}H$(\vec{e},e'p)$ and ^{12}C$(\vec{e},e'p)$ cross sections also required a good understanding of spectrometer detection efficiencies and acceptances, as well as an accurate treatment of radiative corrections [35–37]. A Monte Carlo simulation of the experiment proved to be necessary for the accurate determination of spectrometer acceptances and the treatment of radiative corrections.

In the Monte Carlo calculations, events were weighted by given theoretical cross sections. The ^{2}H responses were supplied by Arenhövel and the ^{12}C responses were supplied by the program PV5FF [38]. The optics of the spectrometers were modeled by second-order matrices. The physical attributes (collimators, vacuum systems, baffles, etc.) of the spectrometers were represented with software collimators. The modeling methodology was derived from the program TURTLE [39].

TABLE VIII. Symbols used in expression for cross section, Eq. (24).

e	=	Electron charge (1.602×10^{-13} μC)
N_{at}	=	Number of atoms per molecule
M_w	=	Molecular weight (g/mole)
N_A	=	Avogadro's number (6.02×10^{23} particles/mole)
ϵ_{ELSSY}	=	ELSSY efficiency
ϵ_{OOPS}	=	OOPS efficiency
l_c	=	Coincidence detection effective target length (cm)
$I(\tau)$	=	Beam current, time dependent (μA)
$\rho(\tau)$	=	Target density, time dependent (g/cm^3)
τ	=	Measurement time (s)
τ_m	=	Total measurement time (s)
N_c	=	Number of true coincidence events
t^c_{proc}	=	Fraction of coincidence events processed (live time <1)
$d\omega$	=	Differential of the electron energy (MeV)
$d\Omega_e$	=	Differential of the electron solid angle (sr)
$d\Omega_p$	=	Differential of the proton solid angle (sr)
dT_p	=	Differential of the proton kinetic energy (MeV)
$\epsilon_c(\vec{p}_e,\vec{p}_p)$	=	Coincidence acceptance function; see Sec. III J 1b

Nominally, a coincidence phase-space volume would be given by the product $\Delta\omega\,\Delta\Omega_e\Delta\Omega_p$, where $\Delta\omega$ is the ELSSY energy acceptance (MeV), $\Delta\Omega_e$ is the ELSSY solid-angle acceptance (sr), and $\Delta\Omega_p$ is the OOPS solid-angle acceptance (sr). However, due to the presence of baffles, vacuum flanges, and other aspects of the detector geometry of the spectrometers, as well as the geometrical effects of an extended target, not all of the events whose particles are within the respective bounds will be detected. An acceptance-efficiency correction factor $C^{\text{coin}}_{\text{acc}}$ (defined and described in more detail in Sec. III J 1b) was determined by the Monte Carlo calculations for each kinematic setting.

Radiative tails, radiative corrections, and no radiation were included as separate options. Radiative tails need to be included to determine acceptance corrections. Radiative corrections were included to determine the effects of acceptances on the corrections. No radiation is needed as a baseline for comparison. The radiative tail was modeled in the Monte Carlo program by using the theoretical prescription of Borie and Drechsel [40]. The Monte Carlo randomized k_γ over the range of energies 0.1–30 MeV. Figure 7 shows a comparison between the missing-energy spectra for ^{12}C at 21° derived from the data and from Monte Carlo. (Some strength from the $s_{1/2}$ shell is present above 30 MeV.)

For comparison with data, one must keep in mind the ~1.5-MeV uncertainty in beam energy, which affects all computed kinematic quantities. The theoretical cross sections were folded over the acceptances without including radiative processes. This procedure also yields a baseline cross section for comparison with cross sections that include radiative corrections. The ratio of the unfolded cross section divided by the folded cross section for ^{2}H at the central value of the acceptance was 1.44, 0.62, and 0.81 for the 0°, 21°, and 29° points, respectively.

1. Cross section determination

The full six-fold $A(e,e'p)B$ cross section $d^6\sigma/d\omega\,d\Omega_e d^3\vec{p}_p$ may be written differentially in the kinetic energy T_p as

$$\frac{d^6\sigma}{d\omega\,d\Omega_e d\Omega_p dT_p}=p_p E_p\frac{d^6\sigma}{d\omega\,d\Omega_e d^3\vec{p}_p},\tag{23}$$

and expressed in terms of the measured quantities as

$$\frac{d^6\sigma}{d\omega\,d\Omega_e d\Omega_p dT_p}=\frac{e}{N_{at}}\frac{M_w}{N_A}\frac{1}{\epsilon_{\text{ELSSY}}\epsilon_{\text{OOPS}}}$$

$$\times\frac{1}{l_c\int_{\tau_m}I(\tau)\rho(\tau)d\tau}$$

$$\times\frac{N_c/t^c_{\text{proc}}}{\int\epsilon_c(\vec{p}_e,\vec{p}_p)d\omega\,d\Omega_e d\Omega_p dT_p},$$

$$\tag{24}$$

where the symbols are defined in Table VIII. In this expression, both the current and the target density (e.g., liquid targets) are permitted to vary with time. The total accumulated charge is $Q=\int_{\tau_m}I(\tau)d\tau$.

a. Luminosity. For the liquid deuterium (LD$_2$) target, the density was not constant during the measurement time, due to boiling. Instead, the time integral was approximated with average quantities $\langle I\rangle\langle\rho\rangle\tau_m$ over the total measurement time. The Monte Carlo analysis indicated that the effective coincidence-detection target length l_c was 0.506 ± 0.004 of the full (5.08 cm) length S. The average effective luminosity

$$L' = \frac{\langle I \rangle}{e} l_c \langle \rho \rangle \frac{N_A}{M_w} N_{at} \quad (\text{cm}^{-2}\ \text{s}^{-1}) \tag{25}$$

was approximately 0.89×10^{36}, 1.00×10^{36}, and 0.97×10^{36} cm^{-2} s^{-1} for the $0°$, $21°$, and $29°$ points, respectively.

For the ^{12}C target, the density was constant and the time integral becomes simply ρQ. Also, the effective target length $l_c = S/\cos \theta_t$, where S is the target thickness and θ_t is the angle between the axis normal to the ^{12}C foil and the beam axis.

b. Implementation of the coincidence acceptance. The coincidence acceptance function $\epsilon_c(\vec{p}_e, \vec{p}_p)$ defines the acceptance of the system of two coupled spectrometers. It is unity for every event in the six-dimensional phase space that can be detected by the two-spectrometer system, and zero for all other events. It depends on the internal geometry and optical characteristics of the spectrometers (and the target geometry, in the case of an extended target) and, when integrated over all phase space, yields the coincidence detection volume. The integration was effected with a Monte Carlo method. The integral extends formally over the entire phase space, but the volume is finite from the definition of $\epsilon_c(\vec{p}_e, \vec{p}_p)$. The rays are chosen randomly to fill all of the phase-space region where $\epsilon_c(\vec{p}_e, \vec{p}_p)$ is unity.

The phase-space integration can be performed in five dimensions in the case of a discrete state in missing energy $[d^6\sigma(E_m) \sim \delta(E_m - \overline{E_m})d^5\sigma]$. Recalling the discussion after Eq. (4) that the responses depend, in general, on four kinematic variables, p_p is now redundant and only three variables are needed. The coincidence cross section reduces to a five-fold differential form as

$$\frac{d^5\sigma(\overline{E_m})}{d\omega\, d\Omega_e d\Omega_p} = \int \frac{d^6\sigma(E_m)}{d\omega\, d\Omega_e d^3\vec{p}_p} p_p^2 \frac{dp_p}{dE_m} dE_m$$

$$= \frac{E_p p_p}{R} \int \frac{d^6\sigma(E_m)}{d\omega\, d\Omega_e d^3\vec{p}_p} dE_m, \tag{26}$$

where

$$R = 1 - \frac{E_p}{E_B} \frac{\vec{p}_p \cdot \vec{p}_m}{p_p^2} \tag{27}$$

is a recoil factor which reduces to unity when the kinetic energy of the residual nucleus is negligible. When the six-fold cross section for a proton knocked out of a discrete state is written as a differential in T_p,

$$\frac{d^6\sigma}{d\omega\, d\Omega_e d\Omega_p dT_p} = R\, \delta(E_m - \overline{E_m}) \frac{d^5\sigma}{d\omega\, d\Omega_e d\Omega_p}, \tag{28}$$

Eq. (26) becomes

$$\int \frac{d^6\sigma}{d\omega\, d\Omega_e d\Omega_p dT_p} dE_m = R(\overline{E_m}) \frac{d^5\sigma(\overline{E_m})}{d\omega\, d\Omega_e d\Omega_p} \tag{29}$$
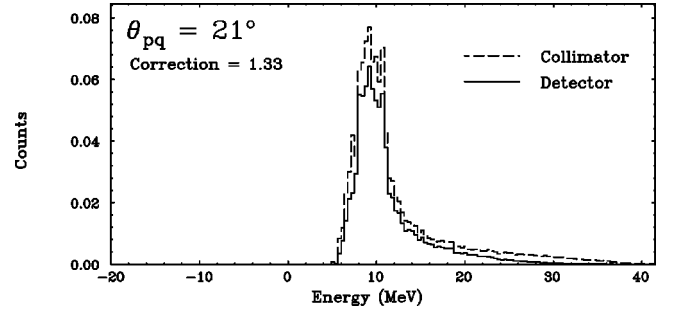
FIG. 8. A comparison between a ^{2}H missing-energy spectrum just after the front collimators of the OOPS to the missing-energy spectrum at the rear detectors.

where, after the integration, $\vec{p}_B$ is constrained from $\vec{p}_p$ to give $E_m = \overline{E_m}$.

The general procedure described above was applied in the two reactions studied. In each case, the integral over the coincidence function $\epsilon_c(\vec{p}_e, \vec{p}_p)$ was replaced with the product of the finite spectrometer acceptances $\Delta\omega\,\Delta\Omega_e\Delta\Omega_p$ and an acceptance correction factor $C_{\text{acc}}^{\text{coin}}$ according to

$$\int \epsilon_c(\vec{p}_e, \vec{p}_p)d\omega\, d\Omega_e d\Omega_p = \frac{\Delta\omega\,\Delta\Omega_e\Delta\Omega_p}{C_{\text{acc}}^{\text{coin}}}. \tag{30}$$

For the ^{2}H$(\vec{e}, e'p)$ reaction, the coincidence acceptance was implemented in the five-dimensional phase space $d\omega\, d\Omega_e d\Omega_p$ because $E_m = \overline{E_m} = 2.224$ MeV is fixed. The five-fold cross section was extracted directly. For the ^{12}C$(\vec{e}, e'p)$ reaction, the $s_{1/2}$-shell contribution sits on the radiative tail of the $p_{3/2}$ shell and extends beyond our acceptance in missing energy ($E_m = 0 - 45$ MeV). The six-fold cross section was extracted and integrated over the $p_{3/2}$ peak in missing energy to obtain the five-fold one.

The Monte Carlo calculations determined the ratio of the number of events that were accepted by the solid-angle defining collimators to the number of events that were recorded by the detection systems. Missing-energy spectra were formed from each of these classes of events. A representative comparison between these two sets of spectra for the $21°$ out-of-plane angle ^{2}H measurement is shown in Fig. 8. The correction factors $C_{\text{acc}}^{\text{coin}}$ obtained were 1.25, 1.33, and 2.11 for the $0°$, $21°$, and $29°$ points, respectively. The relatively large correction factor for the $29°$ point is due to the mismatch between the accepted proton momenta and the out-of-plane angles, and the fact that proton momenta and out-of-plane angles are correlated. For ^{12}C the correction values were 1.12 for $21°$, and 1.11 and 1.27 for the $29°$ point (for the 200-mg and 600-mg targets, respectively).

c. ^{2}H singles cross section. The single-arm three-fold $A(e, e')$ cross section is written in terms of measured quantities as

TABLE IX. Target thickness and ^{2}H$(e,e'p)$ cross sections for each out-of-plane angle, scaled to $\sigma_{(e,e')}$ cross sections and acceptance corrected by Monte Carlo calculations. A 5% systematic uncertainty must be added to the quoted statistical errors.

θ_{pq}	t (mg/cm^2)	$\sigma_{(e,e'p)}$ (nb/MeV sr^2)	$\sigma_{(e,e'p)}/\sigma^{th}_{(e,e'p)}$
0°	592.9 $\pm$ 2.8	249.00 $\pm$ 1.5	1.3
20.9°	587.7 $\pm$ 0.8	3.64 $\pm$ 0.06	1.1
29°	639.0 $\pm$ 0.8	1.00 $\pm$ 0.06	1.7

$$\frac{d^3\sigma}{d\omega\, d\Omega_e dT_p} = \frac{e}{N_{at}} \frac{M_w}{N_A} \frac{1}{\epsilon_{\text{ELSSY}}}$$

$$\times \frac{1}{l_e \int_{\tau_m} I(\tau)\rho(\tau)d\tau} \frac{N_{es}/t^e_{\text{proc}}}{\int \epsilon_c(\vec{p}_e)d\omega\, d\Omega_e},$$

(31)

where l_e is the electron-detection effective target length (cm), N_{es} is the number of single electron events recorded, t^e_{proc} is the fraction of single-electron events processed (live time <1), $\epsilon_c(\vec{p}_e)$ is the single-arm acceptance function (see Sec. III J 1b), and other quantities are the same as those of the coincidence measurement.

The single-arm cross section was determined only in the ^{2}H(e,e') reaction as a luminosity monitoring quantity. Making the same approximations in the luminosity time integral as in the ^{2}H$(\vec{e},e'p)$ coincidence cross section and by using the fact that ELSSY could see all of the target linear dimension ($l_e = S$), we arrive at the following expression for the three-fold cross section:

$$\frac{d^3\sigma}{d\omega\, d\Omega_e} = \frac{1}{L'\,\tau_m} \frac{C^{\text{ELSSY}}_{\text{acc}}}{\epsilon_{\text{ELSSY}}} \frac{N_{es}/t^e_{\text{proc}}}{\Delta\omega\,\Delta\Omega_e},$$

(32)

where the ELSSY acceptance correction factor

$$\int \epsilon_c(\vec{p}_e)d\omega\, d\Omega_e = \frac{\Delta\omega\,\Delta\Omega_e}{C^{\text{ELSSY}}_{\text{acc}}}$$

(33)

is determined from the Monte Carlo integration described in Sec. III J 1b.

2. ^{2}H$(\vec{e},e'p)$ cross section determination

The absolute cross sections were derived from events in the missing-energy spectra. The precision in the absolute cross-section determination is limited mainly by the systematic errors due to uncertainties in the Monte Carlo model and, in the case of deuterium, by the uncertainty in target thickness. For ^{2}H it was necessary first to correct the coincidence cross section for target-thickness fluctuations by using the electron singles cross section and then correcting for detector efficiencies, spectrometer acceptances, and radiative effects.
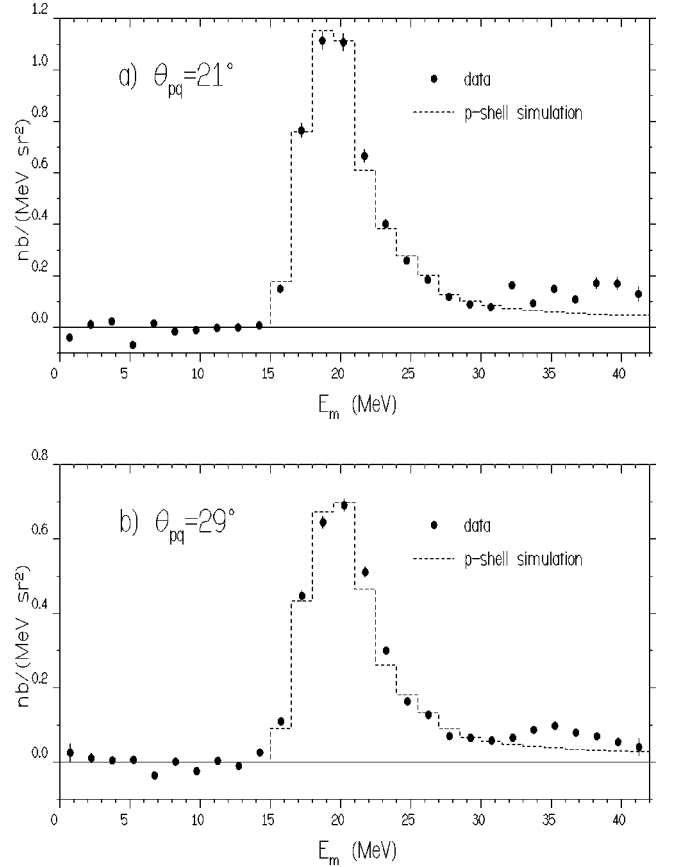

FIG. 9. The ^{12}C cross sections versus missing energy in comparison with Monte Carlo simulations at the two out-of-plane angle settings.

The two spectrometers view the target differently. ELSSY views the entire target while OOPS views only half of the target due to the collimators (see Sec. II). The ELSSY acceptance correction $C^{\text{ELSSY}}_{\text{acc}}$ is a target-acceptance correction combined with the radiative corrections discussed in the previous section. The target-acceptance correction was determined through Monte Carlo methods to be 1.04 for ^{2}H. The overall ELSSY correction factor $C^{\text{ELSSY}}_{\text{acc}}$ was determined to be 1.22 for all out-of-plane angles.

The target thickness for ^{2}H was determined from the measured (e,e') cross section. Equations (32) and (25) were solved for the areal target thickness

$$t = l_e \langle\rho\rangle$$

$$= \frac{N_{es}/t^e_{\text{proc}}}{\Delta\omega\,\Delta\Omega_e} \left(\frac{\langle I\rangle\,\tau_m}{e} \frac{N_A}{M_w} N_{at}\right)^{-1} \frac{C^{\text{ELSSY}}_{\text{acc}}}{\epsilon_{\text{ELSSY}}} \left(\frac{d^3\sigma}{d\omega\, d\Omega_e}\right)^{-1}.$$

(34)

We used (e,e') cross sections that were folded over our electron spectrometer acceptances as determined from Arenhövel's calculation [41], which has been demonstrated to predict existing data very well in this Q^2 region. The cross section for the central value of our kinematics (see Table II) is 18.1 nb/(MeV sr). It becomes 17.3 nb/(MeV sr) when

TABLE X. The fifth response for each out-of-plane angle.

θ_{pq}	^{2}H($\vec{e},e'p$) f'_{LT} (fm^3)	^{12}C($\vec{e},e'p$) p shell f'_{LT} (fm^3)
0°	12.6 ±6.6	
20.9°	−0.326±0.366	+0.075 ± 0.036
29°	−0.433±0.345	−0.017 ± 0.025

folded over acceptances. We assign a systematic error of 5% to this normalization procedure based on these cross sections.

Substituting this target thickness [Eq. (34)] into Eq. (24) yields the singles-corrected coincidence cross section. Table IX gives the derived target thickness and scaled ^{2}H($\vec{e},e'p$) cross section for each out-of-plane angle. The three ($e,e'p$) cross sections from the data are larger than Arenhövel's predictions by 30%, 10%, and 70% for the 0°, 21°, 29° points, respectively.

3. ^{12}C($\vec{e},e'p$) cross sections

The measured six-fold ^{12}C($e,e'p$) cross sections at $\theta_{pq}=21°$ and $\theta_{pq}=29°$ are shown in Fig. 9 and compared with those from the Monte Carlo simulations. Energy shifts of less than 1 MeV were used to align the simulation and the data at each angle, and the simulation was normalized to the data as described in the previous section. Note that division by the coincidence detection volume increases the height of the s-shell relative to the p-shell peak (refer back to Fig. 7). The extracted five-fold differential cross section integrated over the p-shell strength from the missing energy threshold at 14–28 MeV is 8.82±0.20 for $\theta_{pq}=21°$ and 5.86±0.23 for $\theta_{pq}=29°$.

K. Response extraction

The fifth response is proportional to the electron beam asymmetry multiplied by the absolute cross section for unpolarized electrons $\sigma(\theta_{pq},\phi_{pq})=\Sigma$ [see Eq. (8)], i.e.,

$$f'_{LT}(\theta_{pq})=\frac{A_e(\theta_{pq})\sigma(\theta_{pq},\phi_{pq})}{K\sigma_{\text{Mott}}P_B v'_{LT}\sin\phi_{pq}}. \quad (35)$$

In terms of experimental quantities,

$$f'_{LT}(\theta_{pq})=\frac{A_e\sigma(\theta_{pq},90°)}{K\sigma_{\text{Mott}}P_B v'_{LT}}. \quad (36)$$

Here A_e and σ are folded over acceptances in the data as well as the Monte Carlo, whereas σ_{Mott} and v'_{LT} are calculated at the central value of the ELSSY spectrometer. The error on $f'_{LT}(\theta_{pq})$ is calculated by

$$\delta f'_{LT}=|f'_{LT}|\sqrt{\left(\frac{\delta A_e}{A_e}\right)^2+\left(\frac{\delta\sigma}{\sigma}\right)^2+\left(\frac{\delta P_B}{P_B}\right)^2}. \quad (37)$$

Table X gives the fifth response for each out-of-plane angle.

L. Systematic error

The statistical errors in the measurements completely dominate the systematic errors for both the asymmetry and fifth response. In the absolute cross section measurements, the systematic errors are estimated to be larger than the statistical errors. Some of the largest contributors to systematic errors in these measurements include the spectrometer alignment and absolute efficiencies, the target thickness, imprecise representation by the Monte Carlo model, the beam energy and polarization, and the asymmetry in the helicity-dependent beam charge. Tables XI and XII list some of the largest contributors to systematic errors in the ^{2}H($\vec{e},e'p$) and ^{12}C($\vec{e},e'p$) measurements. In the tables, the column of total fractional systematic errors is formed by summing the systematic errors in quadrature. The fractional errors on f'_{LT} are calculated by summing the errors from the asymmetry and cross section in quadrature. A column of the statistical contribution to the overall error is provided for comparison.

In the ^{2}H measurement we assign a 3% systematic error to the measured spectrometer efficiencies due to the methods used to calculate them [24] (see Secs. III A and III B). We

TABLE XI. Sources of error in the ^{2}H($\vec{e},e'p$) measurement.

Item		Fractional error (%)								
		Spect. align.	Spect. eff.	Tgt thick	Monte Carlo	E_i	P_B	Charge asym.	Total sys.	Total stat.
$\sigma_{(e,e'p)}$	@ 0°	0.7	3.0	5.0	8.0	0.6	–	–	9.9	0.6
$\sigma_{(e,e'p)}$	@ 20.9°	1.0	3.0	5.0	8.0	1.3	–	–	10.0	1.7
$\sigma_{(e,e'p)}$	@ 29°	0.5	3.0	5.0	8.0	1.4	–	–	10.0	6.0
A	@ 0°	1.5	–	–	–	0.3	9.4	0.1	9.5	53.1
A	@ 20.9°	0.6	–	–	–	0.3	9.4	0.1	9.4	112.4
A	@ 29°	0.1	–	–	–	0.1	9.4	0.1	9.4	79.5
f'_{LT}	@ 0°	1.7	3.0	5.0	8.0	0.7	9.4	0.1	13.8	53.1
f'_{LT}	@ 20.9°	1.2	3.0	5.0	8.0	1.3	9.4	0.1	13.7	112.4
f'_{LT}	@ 29°	0.5	3.0	5.0	8.0	1.4	9.4	0.1	13.7	79.7

TABLE XII. Sources of error in the ^{12}C$(\vec{e},e'p)$ measurement.

Item	Fractional error (%)								
	Spect. align	Spect. eff.	Tgt thick	Monte Carlo	E_i	P_B	Charge asym.	Total sys.	Total stat.
σ	3.0	4.0	–	–	3.0	–	–	5.8	<4
A	0.3	–	–	–	0.1	10.0	6.0	11.6	>45

estimate a systematic error of 8% in the Monte Carlo, mainly due to inaccuracies in the Monte Carlo model to reproduce some extended target effects. The target thickness and the electron singles-corrected coincidence cross section relied on the electron singles cross section of Arenhövel, to which we assigned a systematic error of 5% (see Sec. III J 1). Sensitivity to beam energy and alignment were estimated from Arenhövel's calculations. The beam energy was allowed to fluctuate within the ± 1.5 MeV error bars of the measurement (see Sec. III E). The contributions due to alignment error were estimated by varying the θ_{pq} angle within the $\pm 0.05°$ estimate of the OOPS module alignment accuracy [24,31]. Contributions to systematic error from the charge asymmetry and beam polarization (P_B) were taken from Secs. III G and III H, respectively. In Table XIII we provide statistical and systematic errors, respectively, for the ^{2}H$(\vec{e},e'p)$ cross section, the fifth response asymmetry, and the fifth response for each out-of-plane angle.

In the ^{12}C measurement the spectroscopic factors at the two angles agreed and the cross sections calculated at two different OOPS field settings at $\theta_{pq}=29°$ were the same. These results indicate that the systematic errors were not large for ^{12}C. The variation of the ^{12}C cross section within the beam energy uncertainty was about $\pm 2\%$. The beam energy calibration also affects the expected coincidence efficiency and this uncertainty is also about $\pm 2\%$. The spectrometer efficiencies contribute slightly more error. We have assigned an efficiency uncertainty of $\pm 3\%$ to the OOPS efficiency and $\pm 2\%$ to ELSSY. What are harder to calculate are the effects of misalignments; we have assigned a $\pm 3\%$ systematic error to this cause.

In ^{12}C the minimum fractional error in the measured asymmetry at the three angles is 46%. This error is to be compared with a 10% systematic error in the beam polarization measurement. We tested the sensitivity of the asymmetry to the beam energy. Within the ± 1.5-MeV error bars of this experiment, the systematic error associated with beam energy at $\theta_{pq}=21°$ is negligible. Misalignments, moreover, treat each polarization identically and only contribute to systematic error by a slight shift of the kinematics. We estimate this effect to be no larger than 0.3% in the fractional error at $\theta_{pq}=21°$.

TABLE XIII. Statistical and systematic errors, respectively, for the ^{2}H$(\vec{e},e'p)$ cross section, the fifth response asymmetry, and the fifth response for each out-of-plane angle. The cross sections are given in units of nb/(MeV sr^2) and the responses are given in units of fm^3.

$\sigma_{(e,e'p)}$	@ 0°	$249.00 \pm 1.50 \pm 24.90$
$\sigma_{(e,e'p)}$	@ 20.9°	$3.64 \pm 0.06 \pm 0.36$
$\sigma_{(e,e'p)}$	@ 29°	$1.00 \pm 0.06 \pm 0.10$
A	@ 0° $(\times 10^2)$	$+1.87 \pm 0.99 \pm 0.18$
A	@ 20.9° $(\times 10^2)$	$-3.07 \pm 3.45 \pm 0.29$
A	@ 29° $(\times 10^2)$	$-13.80 \pm 10.97 \pm 1.29$
f'_{LT}	@ 0°	$+12.6 \pm 6.6 \pm 1.8$
f'_{LT}	@ 20.9°	$-0.326 \pm 0.366 \pm 0.045$
f'_{LT}	@ 29°	$-0.433 \pm 0.345 \pm 0.059$

IV. RESULTS

A. The carbon results

A summary of the ^{12}C$(\vec{e},e'p)$ results from this experiment is given in Table XIV. The asymmetry at $\theta_{pq}=21°$ is two standard deviations from zero, while the point at $\theta_{pq}=29°$ is consistent with zero. The cross sections at both angles are measured to an accuracy of about 7%, including systematic error. Before making comparisons between measured and predicted quantities, the effects of kinematical averaging over the experimental acceptances had to be considered. In particular, the vertical (out-of-plane) acceptance of the electron spectrometer was quite large; a range of roughly 14° in the angle θ_{pq} was spanned at each point. We gauged the effects of acceptance averaging through the Monte Carlo simulations.

The effects of acceptance averaging for the asymmetry and the fifth response were found to be much smaller than the statistical errors reported for the measurements in Table XIV. Thus, no acceptance correction is needed for a comparison of these measured quantities with predicted values. This situation is not the case for the cross-section measurements where averaging reduces the unpolarized cross section by 10% at the 21° point. This effect is much larger than the experimental error bars. Therefore, the measured cross sections, corrected for radiative effects, are compared to the theoretical cross sections corrected for acceptance averaging. Relative to a DWIA calculation with the Schwandt optical potential [42], the measured cross sections at 21° and 29° are smaller by factors of 0.64 and 0.65, respectively. Error bars of 10% on this quantity reflect the approximate variation in theoretical models. The extracted spectroscopic factor, which is multiplied by the number of p-shell protons, is then 2.56 ± 0.25. This value is consistent with earlier measurements of

TABLE XIV. Summary of results for the ^{12}C p shell.

θ_{pq}	$d^5\sigma/(d\omega/d\Omega_e d\Omega_p)$ (nb/MeV sr^2)	$d^5\sigma_{meas}/d^5\sigma_{theory}^{folded}$	A	f'_{LT} (fm^3)
20.9°	$8.8 \pm 0.2 \pm 0.5$	0.64 ± 0.06	$+0.097 \pm 0.045$	$+0.075 \pm 0.036$
29°	$5.9 \pm 0.2 \pm 0.4$	0.65 ± 0.07	-0.032 ± 0.047	-0.017 ± 0.025

2.48 ± 0.38 at Bates [43], 2.26 ± 0.23 at NIKHEF [32,44], and 2.5 at Saclay [45].

A comparison of the measured asymmetries and fifth responses with nonrelativistic, optical-model calculations obtained with the program PV5FF of the Pavia group [38] is given in Fig. 10. The potentials are those of Schwandt *et al.* (*S*) [42], Comfort and Karp (CK) [46], Giannini and Ricco (GR) [47], and Jackson and Abdul-Jalil (JA) [48]. All of these calculations employ the bound-state wave function of Elton and Swift [49] except for the Giannini and Ricco prediction, which uses a consistent wave function derived by the same authors. The PWIA results are, of course, zero at all angles.

A spectroscopic factor of 0.64, as determined by this experiment, has been applied to each model to enable a comparison of our data to predictions for the fifth response; this factor cancels in the asymmetry. The spread in the optical-model predictions for the asymmetries and fifth responses is much larger than that which was found for the cross sections. In particular, the prediction of the JA potential is well separated from the other calculations, and the data point at $\theta_{pq} = 21°$ appears to argue against it. The predictions of the other three potentials are more compatible with the measured points. Clearly, data with higher statistical precision are needed to further constrain such optical model calculations.

Final-state interactions are expected to be large in parallel kinematics. At small angles, however, the fifth response must vanish with the phase-space factor $\sin(\theta_{pq})$. The curves in Fig. 10 are consistent with expectation; the fifth response and the asymmetry rise rapidly from zero to a maximum at small
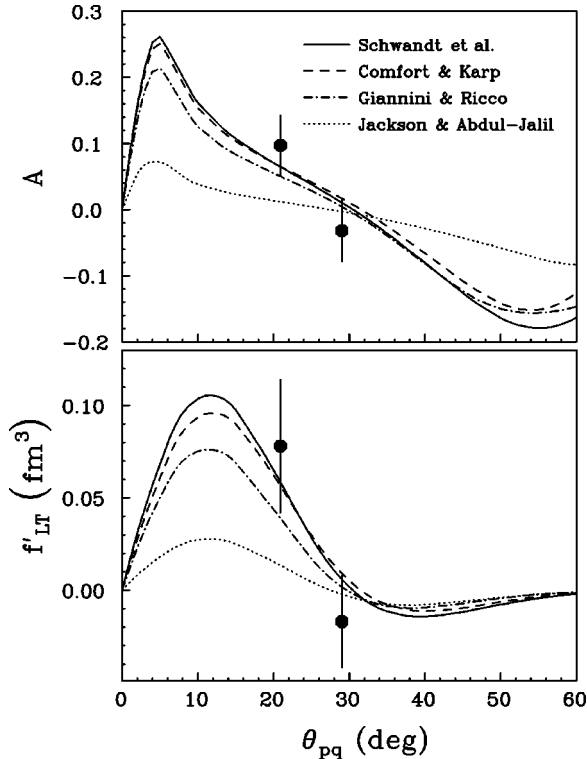

FIG. 10. The measured ^{12}C asymmetry and fifth response in comparison with DWIA predictions based on four optical potentials referenced in the text.

angles. The curves go through zero at roughly $\theta_{pq} = 29°$. This point corresponds to a relative angle of $90°$ between the proton and the residual nucleus in the final state. For all angles, the contributions of meson-exchange currents and/or Δ-isobar configurations were found to be very small. Coulomb distortion of the incident electron wave function was similarly found to produce only a very slight effect on the asymmetry.

All of the aforementioned optical potentials are phenomenological models of commonly used forms [50,51]. The potential parameters were fit to elastic proton scattering cross-section and polarization data over a wide energy range for medium mass target nuclei. The CK parameters were fit to ^{12}C (p,p') data for proton energies between 12 and 180 MeV. The *S* parameters were fit to energies between 80 and 180 MeV for seven nuclei of mass from ^{24}Mg to ^{208}Pb. For a comparison with our measured asymmetries on ^{12}C with 55-MeV protons, the *S* potential is extrapolated in both energy and target mass. However, measurements at NIKHEF have demonstrated that this potential achieves reasonable fits to the data for ^{16}O [52] and ^{12}C [32,44]. The parameters of the GR potential have been fit to proton energies from 20 to 130 MeV for five nuclei of mass from ^{12}C to ^{40}Ca. This parameter search was also constrained by bound-state properties determined from elastic electron scattering. The parameters of JA were fit to ^{12}C data over an energy range of 49 to 156 MeV.

Tables XV and XVI list all the parameters corresponding to $\theta_{pq} = 21°$ for these optical potentials. Each potential includes real and imaginary central terms and a real spin-orbit component; the *S* and JA potentials additionally include very small imaginary spin-orbit contributions. The CK and *S* potentials use volume wells for the imaginary central term, while GR and JA use surface absorption. The *S* and the CK potentials are quite similar in strength and shape. These po-

TABLE XV. Optical-potential central parameters. The potential strengths have units of Mev and distances have units of fm.

	U_v	r_v	a_v	U_v'	r_v'	a_v'	U_s'	r_s'	a_s'
CK	34.7	1.20	0.62	+7.15	1.40	0.68	0.00		
GR	34.8	1.18	0.57	0.00			+9.49	1.13	0.57
S	39.2	1.15	0.69	+6.01	1.47	0.46	0.00		
JA	19.8	1.45	0.55	0.00			+1.45	0.93	0.61

TABLE XVI. Optical-potential spin-orbit parameters. The potential strengths have units of MeV and distances have units of fm.

	U_{so}	r_{so}	a_{so}	U_{so}'	r_{so}'	a_{so}'
CK	5.55[a]	0.93	0.54	0.00		
GR	2.76	1.16	0.57	0.00		
S	6.21	0.96	0.70	+0.05	0.93	0.62
JA	2.77	0.73	0.23	−0.49	1.48	0.64

[a]Note that the sign of this term is opposite that given in the original paper but consistent with the normal use of this potential in the literature.
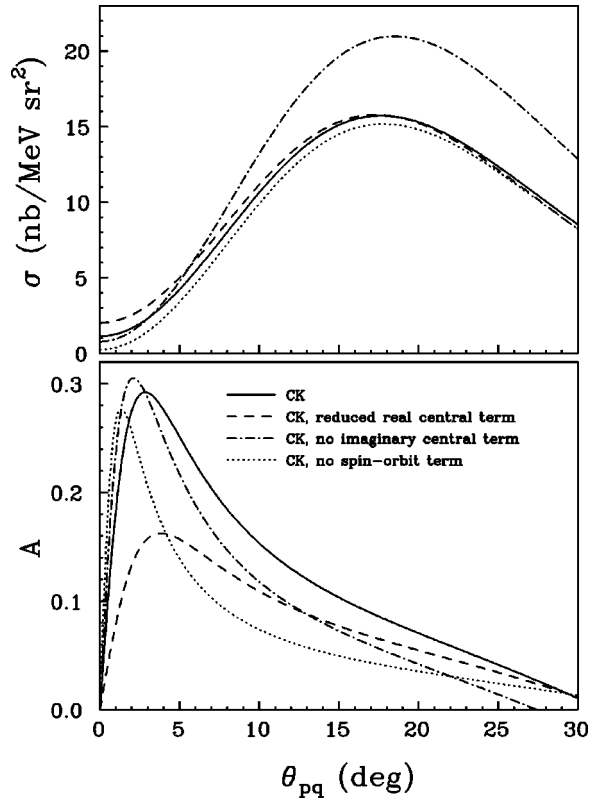
FIG. 11. The sensitivities of the cross section and asymmetry for the $p_{3/2}$ shell in ^{12}C to various parts of the Comfort-Karp optical potential.

tentials differ most at small radii. The JA potential has a much smaller depth of the real and imaginary central wells. The real spin-orbit well of JA is sharply peaked at a radius that is small compared to those of the other potentials. The GR potential produces an asymmetry that is not very different from that of S and CK, yet the shape of its imaginary central well is much different from those potentials, and the depth of its real spin-orbit well is much less.

The contribution of each term in the optical potential to the unpolarized cross section and the asymmetry is shown in Fig. 11. The curves were calculated within DWIA by using the program PV5FF [38]. In the cross section, only the absorbing imaginary central term produces a large effect. In the asymmetry, all terms in the optical potential contribute significantly. Relative to the full CK potential, the asymmetry with no spin-orbit strength is reduced by more than 40% at some angles. Over most of the angular range, the contribution of the imaginary central potential is constant and smaller than that of the real spin-orbit well. When the depth of the real central well is reduced by a factor of 2, the asymmetry is also very strongly affected, particularly at small angles. When an imaginary spin-orbit strength equal to that in the JA potential is applied to CK (this curve is not shown in the figure), the effect is negligible. The much smaller asymmetry produced by JA relative to CK (see Fig. 10) results primarily from the much weaker strengths of the real and imaginary central terms.

Although the data sets, energy ranges, nuclei, and fitting procedures all varied somewhat between the three potentials,

an inescapable drawback of an approach that uses optical models determined from proton elastic scattering is an insensitivity to the nuclear interior [13]. Potentials chosen to reproduce elastic proton scattering describe only the asymptotic behavior of the knock-out proton in $(e,e'p)$, while FSI are sensitive to the component of the proton wave function inside the nucleus. For a study of the valence shell of a relatively light nucleus, such as the p shell of ^{12}C, this point may prove not to be critical. For heavier nuclei, it would not be surprising to see a systematic failure of these potentials.

B. The deuterium results

The most appealing aspect of the deuteron is its simplicity, which allows precise nuclear structure calculations to be performed with controlled approximations. Microscopic calculations based on realistic NN interactions indeed successfully describe much of the available cross-section data for which momentum transfers do not exceed a few hundred MeV/c (or perhaps up to ≈ 1 GeV/c), and also which are not in kinematic regimes where the subnuclear degrees of freedom are expected to contribute significantly. The kinematics of this experiment were chosen to be in such a region.

Separated longitudinal and transverse response functions f_L and f_T have been measured for ^{2}H at Tohoku $[Q^2 = 0.004$ $(\mathrm{GeV}/c)^2]$ [53], NIKHEF $[0.05 \leqslant Q^2 \leqslant 0.27$ $(\mathrm{GeV}/c)^2]$ [54], Saclay $[0.04 \leqslant Q^2 \leqslant 0.40$ $(\mathrm{GeV}/c)^2]$ [55], and Bates $[Q^2 = 0.15$ $(\mathrm{GeV}/c)^2]$ [29,56]. The data have been compared with the results of two microscopic models: (1) nonrelativistic calculations of Arenhövel [57] that are based on the Paris potential [58] and which include the effects of meson exchange currents (MEC) and isobar configurations (IC); and (2) relativistic calculations of Hummel and Tjon [59] in which the strong-interaction and electromagnetic aspects of the reaction are treated consistently. Both calculations provide agreement with the data within $\leqslant 16\%$ on average. The longitudinal-transverse interference response f_{LT} has been extracted for $Q^2 = 0.21$ $(\mathrm{GeV}/c)^2$ at NIKHEF [60], for $Q^2 = 0.15$ $(\mathrm{GeV}/c)^2$ at Saclay [55], and for $Q^2 = 0.15$ $(\mathrm{GeV}/c)^2$ at Bates [29]. The nonrelativistic calculations are substantially below the NIKHEF data, but are consistent with the Saclay and Bates data. The effects of MEC and IC were found to be small [60]. On the other hand, the relativistic calculations are in better agreement with the NI-KHEF data but overpredict the Bates data. Relativistic treatments are needed to describe the forward-backward asymmetries associated with f_{LT} [29]. Apart from some ambiguity about relativistic effects, one can thus anticipate good agreement between this first measurement of the fifth response and the results of conventional nonrelativistic calculations.

We shall present calculations of Arenhövel and co-workers [14,15,57,61,62]. These calculations rely on realistic, phenomenologically adjusted NN interactions, and they have been extensively tested against data at low energies. We should stress, however, that there are very few measurements of separated responses. Therefore, discrepancies between
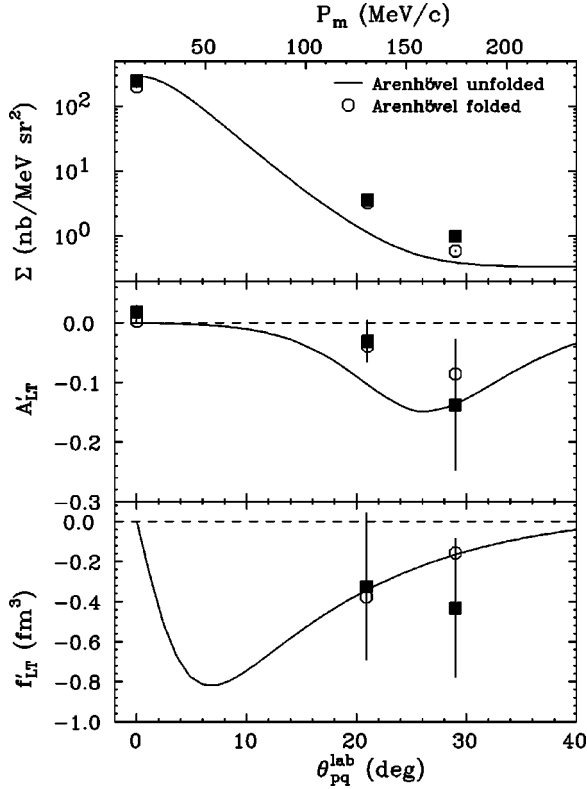
FIG. 12. The unpolarized cross section Σ, asymmetry A, and fifth response f'_{LT} for ^{2}H as calculated with the Paris potential and including MEC and IC [41], plotted as a function of the azimuthal angle θ_{pq} and missing momentum. The data are the experimental values of Table XIII.

conventional theory and exclusive experiments are certainly possible. One should note that, because of the normalization adopted in Eq. (3), the units of f'_{LT} here (fm^3) differ from those (fm) used in our earlier publication [9] and Ref. [14]. All values of f'_{LT} here have been computed from the corresponding cross sections and asymmetries in accordance with Eq. (36).

A plot of the theoretical calculations by Arenhövel [41] for the asymmetry, fifth response, and the coincidence cross section for the kinematics of this measurement (see Table II) is given in Fig. 12. In addition to the contribution of the nucleon-nucleon potential (N), the calculations include the effects of meson exchange currents and isobar configurations. The quantities are plotted as functions of the azimuthal angle θ_{pq} and missing momentum. Our data (solid squares), and the theory folded over the combined angular and momentum acceptances of the two spectrometers (open circles)

are shown. The overall out-of-plane angular acceptance, which was approximately 13° for each datum, proven to have a significant effect on the measured values, as can be seen in Fig. 12. The effect of averaging is substantial and cannot be ignored.

The calculations agree relatively well with the data. The sign, magnitude, and trend of the asymmetry A and fifth response f'_{LT} are in agreement. Due to the size of the uncertainties, a more detailed description and conclusion cannot be drawn. The asymmetry data point in Fig. 12 at $\theta_{pq}=0°$ checks the systematic uncertainty. The fifth response must vanish because of helicity conservation, and the measurement is indeed consistent with zero. One should note that the cross section at the largest reaction angle θ_{pq} has decreased by two orders of magnitude from the point at parallel kinematics as increasingly higher values of missing momenta are probed.

We find that the measured ^{2}H($\vec{e},e'p$) cross sections are 30, 10, and 70 % larger than the non-relativistic predictions of Arenhövel at θ_{pq} values of 0°, 21°, and 29°, respectively, whereas they are 18, 25, and 100 % larger than the Arenhövel predictions with relativistic contributions (RC). The latter are computed consistently in leading order [63]. Similar discrepancies between theory and experiment were observed at NIKHEF for kinematics similar to ours. The measured values of f_L and f_T were determined on average to be larger than Arenhövel's nonrelativistic predictions of these quantities by a factor of 1.15 ± 0.08 and 1.17 ± 0.08, respectively [54]. Our statistical and systematic uncertainties are much smaller than the discrepancies with Arenhövel's theoretical predictions, thus indicating a real effect and the need for more studies on the deuteron as a function of θ_{pq}. Our collaboration is pursuing such studies by employing a technique [5] which will determine all three interference responses simultaneously.

Approximately unfolded values of the cross section, the fifth response, and its asymmetry that can be compared with theoretical predictions given at the central kinematic values are provided in Table XVII. These approximately unfolded values are formed by scaling the measured values of Table XIII by the amount which the theory had changed when folded over acceptances (see Fig. 12).

Arenhövel's calculations [41] which employ four different potential models [58,64–66] for our kinematics are plotted in Fig. 13 against the azimuthal angle θ_{pq} and missing momentum. The data displayed here (solid squares) are the approximately unfolded data of Table XVII. All theoretical predictions, except for the plane-wave Born approximation (PWBA) results which differ substantially from the rest,

TABLE XVII. Measured quantities for each out-of-plane angle for the ^{2}H($\vec{e},e'p$) reaction scaled by the amount that the theoretical values changed by folding over acceptances. Errors shown are statistical only.

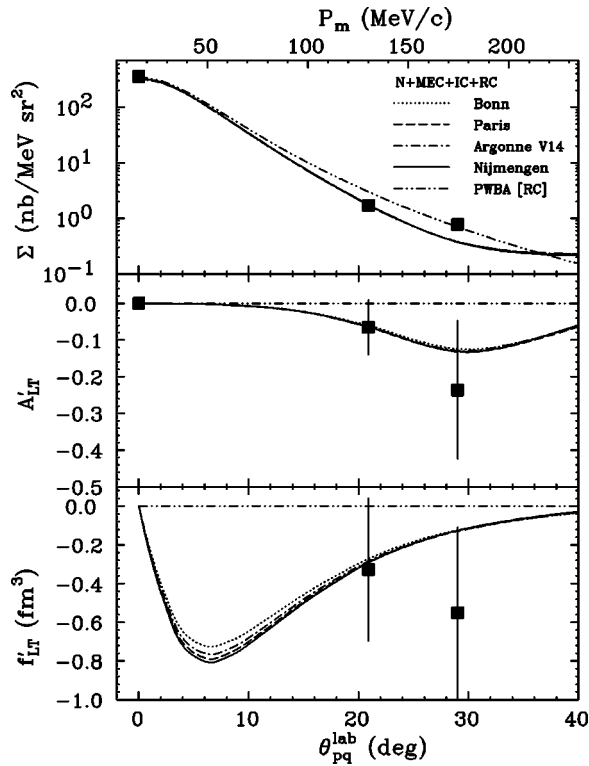| θ_{pq}	$\sigma_{(e,e'p)}$ (nb/MeV sr^2)	A	f'_{LT} (fm^3)
0°	372.00 ± 2.24	0.0 ± 0.0	0.0 ± 0.0
20.9°	1.71 ± 0.03	-0.0657 ± 0.0738	-0.328 ± 0.368
29°	0.744 ± 0.046	-0.236 ± 0.188	-0.551 ± 0.440

FIG. 13. The cross section, asymmetry, and fifth response for ^{2}H calculated with different potentials [41], plotted as a function of the azimuthal angle θ_{pq} and missing momentum. The data are the experimental results that have been approximately unfolded to account for acceptance averaging, corresponding to Table XVII.

FIG. 14. The ^{2}H$(e,e'p)$ cross sections, asymmetry A, and fifth response f'_{LT} from Arenhövel's calculations [41] with the Nijmegen potential. The contributions of the various components are indicated.

agree well with the data for f'_{LT} and A. One finds in Fig. 13 that there is very little sensitivity at these kinematics to the various potential models. This result is not surprising because each model, though constructed differently, was fit to the same precise data, and consequently should yield very similar results at this low momentum transfer.

Details of the results of Arenhövel's calculations for the ^{2}H$(\vec{e},e'p)$ cross sections, A, and f'_{LT}, with the Nijmegen potential and for the kinematics of this measurement, are plotted in Fig. 14. The curves show the contributions of the various pieces which make up the full calculation: the bare NN potential, relativistic contributions meson-exchange currents, and Δ-isobar contributions [63]. It is evident that meson-exchange currents and isobar configurations play a very small role for quasielastic kinematics. It is interesting that relativistic contributions are quite noticeable even at this low momentum transfer [67]. The size of these contributions is roughly the size of the difference in potentials. The coincidence cross section is relatively insensitive to all of these effects; thus the importance of extracting the interference responses to provide a stringent test for nuclear models is easily seen. The noticeable and measurable effect of relativity according to this calculation needs to be pursued further. It may prove that the fifth response and the corresponding asymmetry could provide valuable guidance in elucidating the role of relativity in our understanding of nuclei.
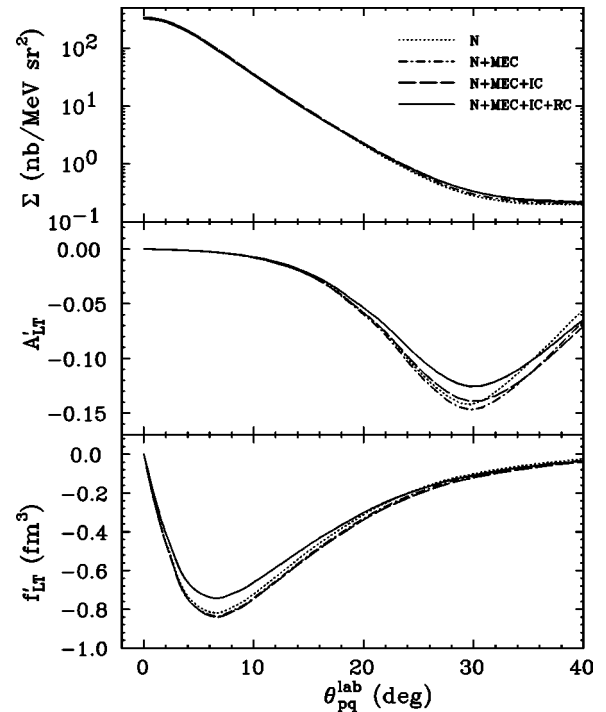
C. Future prospects

The fully developed out-of-plane detection system at Bates will involve four OOPS modules together with a support system which permits them to be arrayed azimuthally about a symmetry axis in the electron scattering plane. Independent asymmetric positioning of the individual spectrometer modules is also possible. The system is specifically tailored for out-of-plane coincidence $(\vec{e},e'p)$ measurements and is optimized for high precision measurements on the nucleon and on few-body nuclear systems. One of the most important capabilities of the OOPS system is the possibility of simultaneous four-fold measurements. This arrangement permits the extraction of important nuclear structure information from asymmetries in the relative coincidence cross sections [5]. Absolute cross-section determinations are not required. In addition, this separation through asymmetries method substantially reduces the magnitude of certain systematic errors.

Many electron scattering laboratories are developing or incorporating out-of-plane capabilities. At the Jefferson Laboratory (JLab), the CEBAF Large Acceptance Spectrometer [68] has out-of-plane detection capability by its very nature. Other spectrometers include the Short Orbit Spectrometer [69] at JLab and Spectrometer B [70] at Mainz. These latter two spectrometers require sequential measurements to extract responses. OOPS is currently the only such spectrometer system that can be positioned symmetrically around q and which is also capable of performing experiments at high luminosity.

V. CONCLUSIONS

We presented in this paper the methodology and the detailed results pertaining to the first measurement of the fifth response function. This response function arises as a result of the interference between two or more complex amplitudes with different phases. As such, it provides an excellent tool for their disentanglement. In the work reported here, both in the case of ^{2}H and ^{12}C, the two dominant interfering contributions are those of direct knockout and of the rescattered outgoing proton. Experimentally the observation of this response function required major accelerator developments such as the availability of polarized electron beams and high duty factor coupled to major detector developments, such as the OOPS system used in the work reported here.

The measurement of the fifth response function f'_{LT} and the corresponding electron helicity asymmetry in ^{2}H and ^{12}C is characterized by large statistical errors but with significantly smaller systematic errors. The latter is an important consideration when assessing the potential of the technique for future measurements. The corresponding cross-section results are of high precision and high statistical accuracy. In the case of ^{12}C, our data yield for the p shell a spectroscopic factor of 0.64 ± 0.06, in agreement with the earlier Saclay and NIKHEF results. In addition, while the high precision cross section measurements cannot distinguish among the equivalent potentials derived from proton scattering data, the fifth response and the corresponding asymmetry show far greater sensitivity. Theoretical predictions indicate discriminating capability in a number of important components of the potential, which cannot be distinguished through cross-section measurements. In the case of ^{2}H our results for the fifth response function and its asymmetry tend to agree with the results of the full nonrelativistic calculation, which employs the Paris potential. However, the corresponding unpolarized cross-section measurements are not well described.

With the technical and methodological problems solved, as this experiment clearly demonstrates, out-of-plane spectrometry provides a novel probe which can yield important new information for both nuclei and hadrons.

[1] T. W. Donnelly and A. S. Raskin, Ann. Phys. (N.Y.) **169**, 247 (1986).

[2] A. S. Raskin and T. W. Donnelly, Ann. Phys. (N.Y.) **191**, 78 (1989).

[3] H. Arenhövel, W. Leidmann, and E. L. Tomusiak, Z. Phys. A **331**, 123 (1988).

[4] S. Boffi, C. Giusti, F. D. Pacati, and M. Radici, *Electromagnetic Response of Atomic Nuclei* (Oxford University Press, Oxford, England, 1996).

[5] C. N. Papanicolas, R. Alarcon, L. S. Cardman, S. Dolfini, R. M. Laszewski, J. Mandeville, S. E. Williamson, S. A. Wood, and A. M. Bernstein, Nucl. Phys. **A497**, 509c (1989).

[6] S. M. Dolfini *et al.*, Nucl. Instrum. Methods Phys. Res. A **344**, 571 (1994).

[7] J. B. Mandeville *et al.*, Nucl. Instrum. Methods Phys. Res. A **344**, 583 (1994).

[8] J. Mandeville *et al.*, Phys. Rev. Lett. **72**, 3325 (1994).

[9] S. Dolfini *et al.*, Phys. Rev. C **51**, 3479 (1995).

[10] S. Boffi, C. Giusti, and F. D. Pacati, Nucl. Phys. **A435**, 697 (1985).

[11] G. Co, A. M. Lallena, and T. W. Donnelly, Nucl. Phys. **A469**, 684 (1987).

[12] B. Frois and C. N. Papanicolas, Annu. Rev. Nucl. Part. Sci. **37**, 133 (1987).

[13] S. Boffi and M. Radici, Nucl. Phys. **A526**, 602 (1991).

[14] H. Arenhövel, W. Leidmann, and E. L. Tomusiak, Phys. Rev. C **46**, 455 (1992).

[15] W. Fabian and H. Arenhövel, Nucl. Phys. **A314**, 253 (1979).

[16] J. M. Laget, Can. J. Phys. **62**, 1046 (1984).

[17] W. Bertozzi, M. V. Hynes, C. P. Sargent, W. Turchinetz, and C. Williamson, Nucl. Instrum. Methods **162**, 211 (1979).

[18] Elgiloy is a nonmagnetic, corrosion resistant, cobalt-nickel alloy.

[19] Kennertium is a machinable tungsten alloy and is a trademark of the Kennemetal corporation.

[20] W. Bertozzi, M. V. Hynes, C. P. Sargent, C. Creswell, P. C. Dunn, A. Hirsch, M. Leitch, B. Norum, F. N. Rad, and T. Sasanuma, Nucl. Instrum. Methods **141**, 457 (1977).

[21] D. Jordan, S. Gilad, M. Holtrop, T. McIlvain, W. Schmitt, and L. Weinstein, Bates Linear Accelerator Center Internal Report No. B/IR 92–03, 1992.

[22] M. Holtrop, D. Jordan, T. McIlvain, V. Bhushan, and L. Weinstein, Bates Linear Accelerator Center Internal Report No. B/IR 92–04, 1992.

[23] W. M. Schmitt, Ph.D. thesis, MIT, 1993.

[24] J. B. Mandeville, Ph.D. thesis, University of Illinois at Urbana–Champaign, 1993.

[25] L. G. Atencio, J. F. Amann, R. L. Boudrie, and C. L. Morris, Nucl. Instrum. Methods Phys. Res. **187**, 381 (1981).

[26] A. H. Walenta, Nucl. Instrum. Methods **151**, 461 (1978).

[27] D. Jordan, W. Bertozzi, V. Bhushan, W. Boeglin, S. Gilad, M. Holtrop, T. McIlvain, and L. Weinstein, Bates Linear Accelerator Center, Internal Report (1992).

[28] D. Toback, S.B. thesis, MIT, 1991.

[29] D. Jordan *et al.*, Phys. Rev. Lett. **76**, 1579 (1996); Ph.D. thesis, MIT, 1994.

[30] V. Bhushan, S.M. thesis, MIT, 1992.

[31] S. M. Dolfini, Ph.D. thesis, University of Illinois at Urbana–Champaign, 1994.

[32] G. van der Steenhoven, H. P. Blok, E. Jans, M. de Jong, L. Lapikas, E. N. M. Quint, and P. K. A. de Witt Huberts, Nucl. Phys. **A480**, 547 (1988).

[33] P. C. Dunn, Nucl. Instrum. Methods **165**, 163 (1979).

[34] J. Arrington, E. J. Beise, B. W. Filippone, T. G. O'Neill, W. R. Dodge, G. W. Dodson, K. A. Dow, and J. D. Zumbro, Nucl. Instrum. Methods Phys. Res. A **311**, 39 (1992).

[35] L. C. Maximon, Rev. Mod. Phys. **41**, 193 (1969).

[36] L. W. Mo and Y. S. Tsai, Rev. Mod. Phys. **41**, 205 (1969).

[37] H. Überall, in *Electron Scattering From Complex Nuclei–Part B*, Vol. 36 of *Pure and Applied Physics*, edited by H. S. W. Massey and K. A. Brueckner (Academic Press, New York, 1971).

[38] S. Boffi, C. Giusti, and F. D. Pacati (private communication).

[39] D. C. Carey, TURTLE, Fermilab National Accelerator Laboratory Report No. NAL–64, 1978.

[40] E. Borie and D. Drechsel, Nucl. Phys. **A167**, 369 (1971).

[41] H. Arenhövel (private communication).

[42] P. Schwandt, H. O. Meyer, W. W. Jacobs, A. D. Bacher, S. E. Vigdor, M. D. Kaitchuck, and T. R. Donoghue, Phys. Rev. C **26**, 55 (1982).

[43] L. B. Weinstein, Ph.D. thesis, MIT, 1988.

[44] G. van der Steenhoven, Ph.D. thesis, Vrije Universiteit te Amsterdam (NIKHEF), 1987.

[45] J. Mougey, M. Bernheim, A. Bussière, A. Gillebert, Phan Xuan Hô, M. Priou, D. Royer, I. Sick, and G. J. Wagner, Nucl. Phys. **A262**, 461 (1976).

[46] J. R. Comfort and B. C. Karp, Phys. Rev. C **21**, 2162 (1980).

[47] M. M. Giannini and G. Ricco, Ann. Phys. (N.Y.) **102**, 458 (1976).

[48] D. F. Jackson and I. Abdul-Jalil, J. Phys. G **6**, 481 (1980).

[49] L. R. B. Elton and A. Swift, Nucl. Phys. **A94**, 52 (1967).

[50] M. Bernheim *et al.*, Nucl. Phys. **A375**, 381 (1982).

[51] S. Frullani and J. Mougey, in *Single-particle Properties of Nuclei through* $(e,e'p)$ *Reactions*, Vol. 14 of *Advances in Nuclear Physics*, edited by J. W. Negele and E. Vogt (Plenum Press, New York, 1984).

[52] M. B. Leuschner, Ph.D. thesis, University of New Hampshire, 1992.

[53] T. Tamae, H. Kawahara, A. Tanaka, M. Nomura, K. Namai, M. Sugawara, Y. Kawazae, H. Tsubota, and H. Miyase, Phys. Rev. Lett. **59**, 2919 (1987).

[54] M. van der Schaar *et al.*, Phys. Rev. Lett. **66**, 2855 (1991).

[55] J. E. Ducret *et al.*, Nucl. Phys. **A553**, 697c (1993).

[56] T. McIlvain, Ph.D. thesis, MIT, 1994.

[57] H. Arenhövel, Nucl. Phys. **A384**, 287 (1982).

[58] M. Lacombe, B. Loiseau, J. M. Richard, R. Vinh Mau, J. Côté, P. Pirès, and R. de Tourreil, Phys. Rev. C **21**, 861 (1980).

[59] E. Hummel and J. A. Tjon, Phys. Rev. Lett. **63**, 1788 (1989); Phys. Rev. C **42**, 423 (1990).

[60] M. van der Schaar *et al.*, Phys. Rev. Lett. **68**, 776 (1992).

[61] G. Beck and H. Arenhövel, Few-Body Syst. **13**, 165 (1992).

[62] T. Wilbois, G. Beck, and H. Arenhövel, Few-Body Syst. **17**, 91 (1994).

[63] F. Ritz, H. Göller, T. Wilbois, and H. Arenhövel, Phys. Rev. C **55**, 2214 (1997).

[64] M. M. Nagels, T. A. Rijken, and J. J. de Swart, Phys. Rev. D **17**, 768 (1978).

[65] R. B. Wiringa, R. A. Smith, and T. L. Ainsworth, Phys. Rev. C **29**, 1207 (1984).

[66] R. Machleidt, K. Holinde, and C. Elster, Phys. Rep. **149**, 1 (1987).

[67] B. Mosconi and P. Ricci, Nucl. Phys. **A517**, 483 (1990).

[68] CEBAF Hall B conceptual design report, 1990.

[69] H. E. Jackson, in *CEBAF Summer Workshop*, 1992, edited by F. Gross and R. Holt, AIP Conf. Proc. No. 269 (AIP, New York, 1992), p. 438.

[70] E. A. J. M. Offermann (private communication).